

The genesis of the ores and intrusions at the Yuhai Cu–Mo deposit in eastern Tianshan, NW China: Constraints from geology, geochronology, geochemistry, and Hf isotope systematics

Yin-Hong Wang ^{*}, Fang-Fang Zhang, Jia-Jun Liu

State Key Laboratory of Geological Processes and Mineral Resources, China University of Geosciences, Beijing 100083, China



ARTICLE INFO

Article history:

Received 23 November 2015

Received in revised form 29 February 2016

Accepted 1 March 2016

Available online 12 March 2016

Keywords:

Zircon U–Pb dating

Molybdenite Re–Os dating

Geochemistry

Hf isotope

Yuhai porphyry Cu–Mo deposit

Eastern Tianshan

ABSTRACT

The Yuhai porphyry Cu–Mo deposit is located in the eastern Tianshan orogenic belt of the southern Central Asian Orogen Belt, being an economically important porphyry Cu deposit in NW China. The deposit comprises sixteen buried orebodies that are predominantly associated with dioritic and granodioritic intrusions and are structurally controlled by roughly NE-trending faults. LA-ICP-MS zircon U–Pb dating yielded crystallization ages of 441.6 ± 2.5 Ma (MSWD = 0.03, n = 24) for diorite and 430.4 ± 2.9 Ma (MSWD = 0.04, n = 19) and 430.3 ± 2.6 Ma (MSWD = 0.09, n = 24) for granodiorite. In situ zircon Hf isotope data on a diorite sample show $\varepsilon_{\text{Hf}}(t)$ values from +8.7 to +18.6, and two granodiorite samples exhibit similar $\varepsilon_{\text{Hf}}(t)$ values from +12.6 to +19.6 and +12.6 to +18.9, respectively. The dioritic and granodioritic intrusions belong to a low-K tholeiite series and are relatively enriched in large ion lithophile elements (K, Ba, Pb, and Sr) and are depleted in high field strength elements (Th, Nb, Ta, and Ti). Moreover, these intrusions have high SiO₂, Al₂O₃ and MgO contents, low Na₂O, P₂O₅ and TiO₂ contents, low Nb/Ta ratios, and slightly positive Eu anomalies. Re–Os dating of molybdenite intergrowth with chalcopyrite yielded a well-constrained $^{187}\text{Re}–^{187}\text{Os}$ isochron age of 351.7 ± 2.9 Ma (MSWD = 1.5) with a weighted average age of 355.7 ± 2.4 Ma (MSWD = 0.69) Ma, indicating that the Yuhai Cu–Mo deposit is younger than the intrusion of the diorite and granodiorite. Combined with the regional geological history and above-mentioned data, we suggest that the Yuhai intrusions were most likely derived from the partial melting of mantle components that were previously metasomatized by slab melts formed by the northward subduction of the ancient Tianshan ocean plate beneath the Dananhu–Tousuquan island arc during the Silurian to Carboniferous. Under the subduction-related tectonic setting, the metasomatized mantle magma was emplaced into the shallow crust and induced the formation of the Early Carboniferous Yuhai Cu–Mo deposit, and the hydrothermal fluids of enriched sulfides probably played an important role in the Cu–Mo mineralization.

© 2016 Elsevier B.V. All rights reserved.

1. Introduction

The Central Asian Orogenic Belt (CAOB) is one of the largest Phanerozoic accretionary orogens in the world (Windley et al., 2007; Xiao and Santosh, 2014; Zhao et al., 2015). The formation of the CAOB is considered to be a result of the Paleo-Asian Ocean closure, involving lateral accretion of island arcs, ophiolites, oceanic islands, seamounts, accretionary wedges, oceanic plateaus and microcontinents (Sengör et al., 1993; Cawood et al., 2009; Xiao et al., 2015a). The west–east trending eastern Tianshan orogenic belt, which is located along the southern margin of the CAOB (Fig. 1A, B; Chen et al., 2012b; Huang et al., 2013), is one of the most important tectonic–magmatic–metallogenic belt in China (Xiao et al., 2004, 2010; Deng et al., 2014, 2015a; Wang et al.,

2014, 2015a) and experienced a complex tectonic evolution including subduction, accretion and the subsequent collision between the Siberian Craton to the north and the Tarim Craton to the south (Mao et al., 2014; Pirajno, 2010, 2013; Tang et al., 2015; Xue et al., 2014, 2015). Thus eastern Tianshan represents a key area for understanding the tectonic evolution of the CAOB. According to previous studies, widespread magmatism has taken place in the eastern Tianshan orogenic belt, which is characterized by voluminous Paleozoic granitoid intrusions (Zhou et al., 2010; Pirajno et al., 2011; Wang et al., 2015b, c). The formation of numerous metal deposits were closely associated with the Paleozoic magmatic hydrothermal activity in eastern Tianshan, including the Tuwu–Yandong Cu deposit (Shen et al., 2014; Wang et al., 2015b, c), Chihu Cu deposit (Wu et al., 2006b; Zhang et al., 2015b), Sanchakou Cu deposit (Qin et al., 2009), Hongshi Au deposit (Pirajno et al., 1997, 2011; Wang et al., 2016a), Yamansu Fe–Cu deposit (Hou et al., 2014) and Weiquan Ag–Cu deposit (Han et al., 2006).

The Yuhai Cu deposit located within the northeastern part of the eastern Tianshan (Fig. 1C), Xinjiang, China, is one of the economically

^{*} Corresponding author at: State Key Laboratory of Geological Processes and Mineral Resources, China University of Geosciences, 29 Xue-Yuan Road, Haidian District, Beijing 100083, China.

E-mail address: wyh@cugb.edu.cn (Y.-H. Wang).

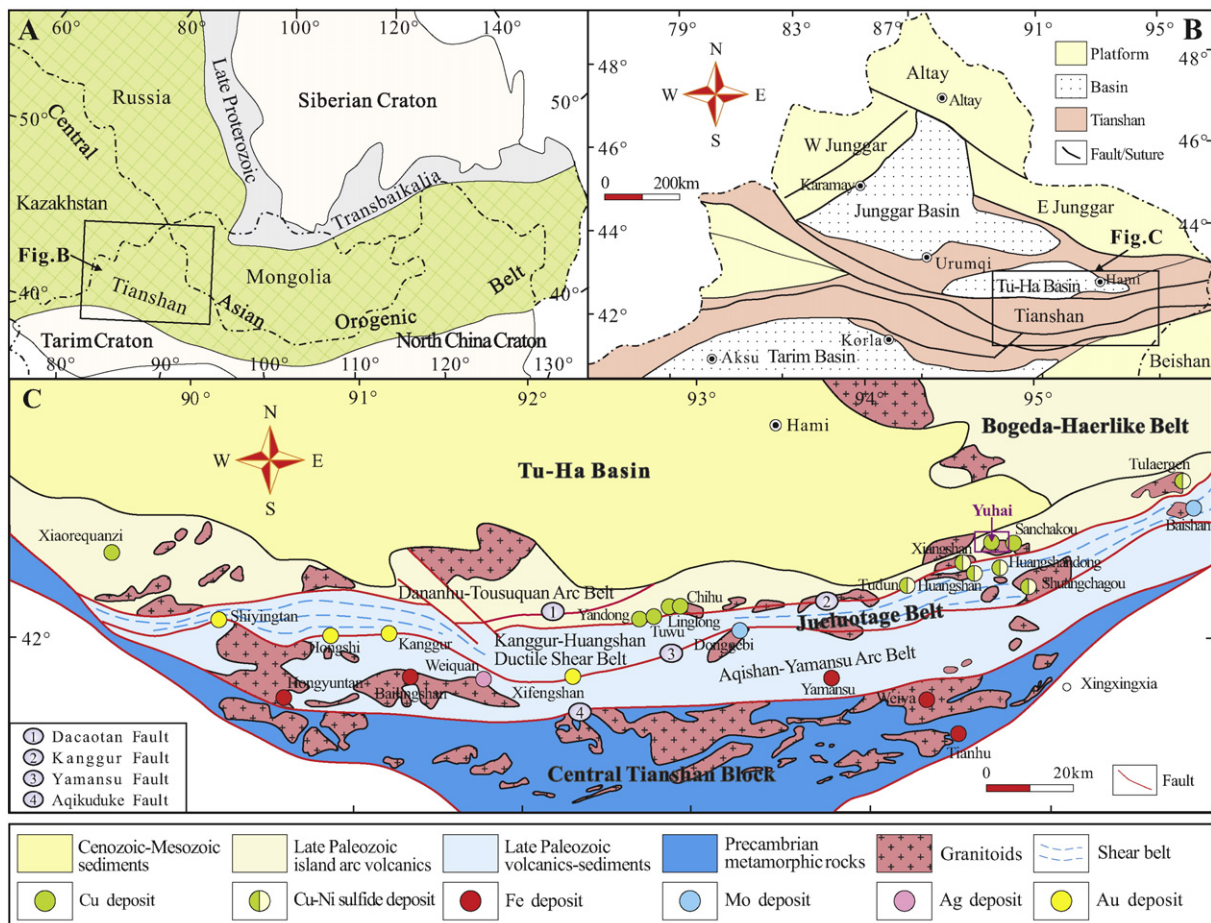


Fig. 1. (A) Location of the study area in the Central Asian Orogenic Belt. (B) Sketch map showing the geological units of the Tianshan Belt. (C) Simplified geological map of the eastern Tianshan Belt.
Panel A is modified from Jahn et al. (2000). Panel B is modified from Chen et al. (2012b). Panel C is modified from Huang et al. (2013).

most important porphyry Cu area in the province. It was first identified in 2011 during an assessment of geochemical anomalies by the No. 704 Geological Team of the Xinjiang Nonferrous Geoexploration Bureau, and the detailed geological mapping and lab-based research undertaken during this period suggested that this was a porphyry deposit that was spatially and potentially genetically associated with the diorite and granodiorite. To date, however, only minimal basic geological research has been undertaken in this area (Zang, 2014; Wei, 2015), which means that the ore-forming processes, tectonic settings and ages of the ore-forming related intrusions are all unclear. In this study, we present new LA-ICP-MS zircon U-Pb dating, whole-rock geochemical data, in situ zircon Hf isotopic compositions and molybdenite Re-Os ages to constrain the magma source of intrusions and the timing of mineralization in the Yuhai deposit and to further explore their genetic relationships and tectonic settings. This study provides new information on the prospectivity of this area and the wider eastern Tianshan orogenic belt for porphyry Cu mineralization.

2. Geological setting

2.1. Regional geology

The eastern Tianshan orogenic belt is a typical Paleozoic island arc system characterized by a complex tectonic history and diverse styles of mineral systems (Zhai et al., 1999, 2011; Charvet et al., 2007; Xiao et al., 2010, 2013; Chen et al., 2012a; Pirajno, 2013). It can be divided into three major tectonic zones: the Bogeda-Haerlike belt, the Jueluotage belt and the Central Tianshan block from the north to the south (Fig. 1C).

These tectonic zones have different rock associations and host distinct mineralizations (Pirajno et al., 2011; Qin et al., 2011; Chen et al., 2012b). The Bogeda-Haerlike belt comprises well-developed Ordovician-Carboniferous volcanic rocks, granites and mafic-ultramafic intrusions and contains only few porphyry Cu and Au prospects. The Jueluotage belt is characterized by Paleozoic volcanic and sedimentary rocks that are intruded by voluminous Carboniferous-Permian felsic and mafic-ultramafic complexes (Zhou et al., 2010; Gao et al., 2015; Wang et al., 2015a, 2016a). The Central Tianshan block is comprised of Precambrian basement and hosts some hydrothermal magnetite deposits (Bgmrxuar, 1993; Qin et al., 2011; Shen et al., 2014). The main structures of eastern Tianshan are characterized by a series of approximately EW-trending faults including the Dacaotan, Kanggur, Yamansu and Aqikuduke faults (Fig. 1C; Ma et al., 1993; Huang et al., 2013; Wang et al., 2015d).

The Jueluotage belt can be subdivided into the Wutongwozi-Xiaorequanzi and Dananhu-Tousuquan arcs in the north, the Kanggur-Huangshan ductile shear zone in the center and the Aqishan-Yamansu arc in the south, which are separated by the Kanggur and Yamansu faults (Fig. 1C). The lithologies exposed in the study area include the Lower Carboniferous Kushui, Yamansu and Gandun formations (Zhang et al., 2003, 2008; Xiao et al., 2013; Wang et al., 2016b). The Kushui Formation is composed of mainly turbiditic graywacke and sandstone. The Yamansu Formation comprises a suite of intermediate to felsic calc-alkaline volcanic lavas, pyroclastic and sedimentary rocks. The Gandun Formation is composed of turbidites with minor limestone and volcanic rocks.

Widespread intrusive and subvolcanic rocks including diorite porphyry, quartz diorites, plagiogranites, monzogranites, syenogranites

and mafic-ultramafic bodies were primarily emplaced during the Silurian to Permian (Zhou et al., 2010; Su et al., 2012; Zhang et al., 2015a; Zhao et al., 2015) and are located in a nearly EW-trending band along the Dananhu-Tousuquan arc (Fig. 1C). In the Dananhu-Tousuquan arc, EW-trending faults include the Dacaotan and Kanggur faults. NW and NE trending faults are also found in the region (Shen et al., 2014; Gao et al., 2015). Several porphyry Cu deposits (e.g., Fuxing, Tuwu, Yandong, Linglong and Chihu) were formed along the southern margin of the Dananhu-Tousuquan arc; such deposits are mainly related to plagiogranite porphyries as well as to deep faults (Fig. 1C).

2.2. Ore deposit geology

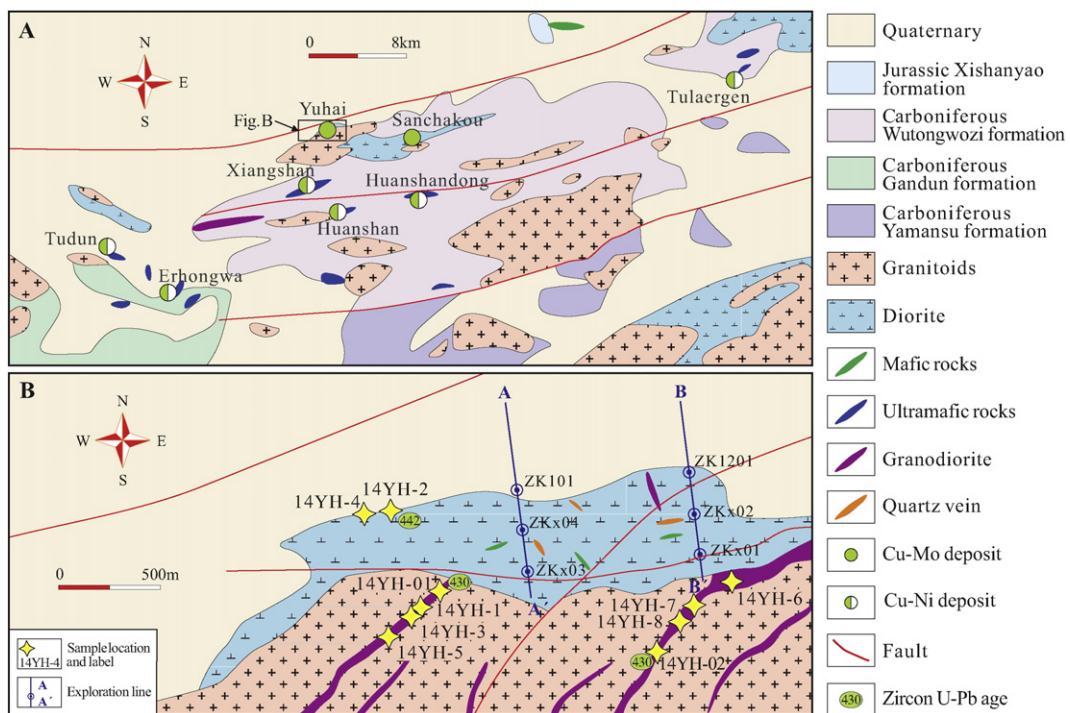
The Yuhai porphyry Cu-Mo deposit is situated in the eastern part of the Dananhu-Tousuquan arc belt, approximately 120 km southeast of the Hami City, Xinjiang (Fig. 1C). It is hosted by intermediate-felsic intrusions and volcanic rocks and is located approximately 3–5 km north of the Kanggur fault. The major structures at the Yuhai deposit are NE-trending ductile shear faults that are the secondary faults of the Kanggur-Huangshan ductile shear zone, whereas EW-trending structures are also present within the area (Fig. 2A, B).

In the northern Yuhai area, the rocks contain Lower Carboniferous Wutongwozi Formation spilite-keratophytic series and Neogene Putaogou Formation and Quaternary sediments (Fig. 2A; Zang, 2014; Wei, 2015). In the southern Yuhai area, various granitoid intrusions occur as stocks and dikes that cover an area of approximately 2 km² (Fig. 2A). These intrusions are mainly composed of diorite, granodiorite, diorite porphyry, dacite porphyry and alkali-feldspar granite. Diorite and granodiorite are the primary components of the host rocks in the deposit (Fig. 3A, B). In the study area, the diorite and granodiorite generally exhibit low or moderate degrees of alteration (Fig. 4A, B). The diorite is light gray to gray-white in color and has a microgranular or aphanitic groundmass (Fig. 4A). It exhibits a massive structure that consists of plagioclase (~50%), hornblende (~15%), quartz (~20%), and biotite (~10%) with accessory magnetite, apatite and zircon. The plagioclase is

characterized by a hypidiomorphic, tabular texture with polysynthetic twinning (Fig. 4C). The hornblende is dominated by a xenomorphic tabular texture. The biotite is mainly yellow-brown in color with a hypidiomorphic-xenomorphic flaky or fragmental texture. The light gray granodiorite is primarily composed of plagioclase (~45%), hornblende (~20%), quartz (~25%) and biotite (~5%) with accessory magnetite, apatite and zircon. The plagioclase is dominated by oligoclase and andesine and is hypidiomorphic-xenomorphic (Fig. 4D), whereas the hornblende is characterized by a hypidiomorphic, tabular texture.

In the Yuhai porphyry Cu-Mo deposit, 16 buried orebodies have been identified (Fig. 3A, B) that contain more than 0.3 Mt Cu and 3870 t Mo (Zang, 2014; Wei, 2015) and are still in the exploration stage. The orebodies mainly occur as veins that are 100–1500 m long and 1–44 m thick and dip toward the south at an angle of 10°. In the dipping direction, the explored orebodies extend down-dip for more than 600 m (Wei, 2015), and the Cu-Mo mineralization occurs predominantly in diorite and granodiorite. Sulfide mineralization in the Yuhai deposit occurs as both disseminations and veinlets (Fig. 4E, F). The ore minerals are dominated by chalcopyrite and pyrite (Fig. 4G) with minor molybdenite, bornite, sphalerite (Fig. 4H), malachite, hematite and chalcocite. The gangue minerals are composed of quartz, sericite, and chlorite with minor biotite, epidote and calcite.

The Yuhai deposit shows a zonation of alteration and mineralization, which is the case for the majority of porphyry deposits. The Cu-Mo mineralization is associated with potassic, chlorite-sericite, phyllitic and propylitic alteration in diorite and granodiorite. The lack of potassic alteration at the surface within the deposit indicates that the area has undergone minimal erosion and that the deposit is largely preserved. Based on the alteration mineral assemblages and ore fabrics as well as on crosscutting relationships, the Cu-Mo mineralization of the Yuhai deposit can be divided into four stages. Stage I is characterized by vein-like and disseminated mineralization associated with potassic alteration with an assemblage of quartz + pyrite. Stage II is represented by vein stockworks containing quartz + pyrite + chalcopyrite associated with chlorite-sericite-phyllitic alteration. Stage III is characterized by



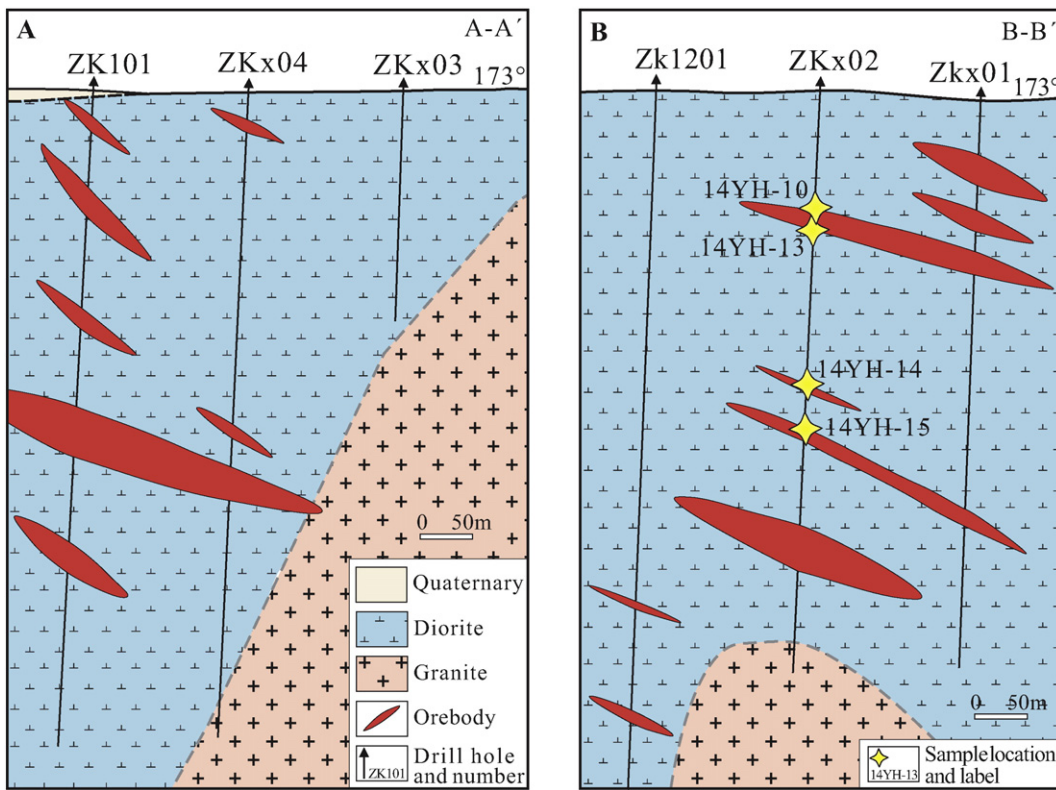


Fig. 3. Geological section of the A-A' and B-B' exploration lines across the Yuhai porphyry Cu-Mo deposit. Modified from Zang (2014).

an assemblage of quartz + chalcopyrite + molybdenite occurring as veins or disseminations in hosting rocks. Stage IV consists of carbonates (calcite) and minor sulfides. Stage III and Stage IV are commonly associated with phyllitic alteration (Zang, 2014; Wei, 2015).

3. Sample preparation and analytical methods

3.1. Sample preparation

The intrusive samples in the Yuhai deposit, especially around the ore body, are generally altered to some degree. In this study, the least altered samples from the Yuhai porphyry Cu-Mo deposit were chosen from outcrops at the surface, and the sampling locations are shown in Fig. 2B. One diorite (14YH-1) and two granodiorite (14YH-01 and 14YH-02) samples were collected for LA-ICP-MS zircon U-Pb dating, trace element and in situ Hf isotopic analyses. One diorite sample (14YH-4) and six granodiorite samples (14YH-1, 14YH-8, 14YH-3, 14YH-5, 14YH-6, and 14YH-7) were chosen for major and trace element analysis. In addition, four molybdenite samples (14YH-13, 14YH-14, 14YH-15 and 14YH-10) were collected from the Cu-Mo orebodies of the Yuhai deposit for Re-Os analyses.

3.2. Analytical methods

3.2.1. Zircon U-Pb dating

Zircon concentrates were separated from the diorite and granodiorite samples by using conventional heavy liquids, magnetic separation techniques, and handpicking under a binocular microscope at the Langfang Regional Geological Survey in Hebei Province, China. Zircon grains, together with zircon standard TEMORA-1 and 91500, were mounted in epoxy mounts, which were then polished to section the crystals in half for analysis. Zircons were documented with transmitted and reflected light micrographs as well as cathodoluminescence (CL) images to reveal their internal structures prior to LA-ICP-MS analyses. LA-ICP-MS zircon

U-Pb dating and trace element analyses were synchronously conducted on an Agilent 7500a ICP-MS, equipped with a 193 nm laser ablation system, housed at the State Key Laboratory of Geological Process and Mineral Resources of the China University of Geosciences, Beijing. During the analyses, the laser spot was 10 μm or 23 μm in different samples. The $^{207}\text{Pb}/^{206}\text{Pb}$ and $^{206}\text{Pb}/^{238}\text{U}$ ratios were calculated using GLITTER program, and then corrected using zircon TEMORA-1 as an external standard. The detailed analytical procedures are similar to those described by Yuan et al. (2004) and Wu et al. (2006a). Error on individual analysis by LA-ICP-MS is quoted at the 1 σ confidence level. The results were processed using the ISOPLOT software (Ludwig, 2003).

3.2.2. Whole rock major and trace element compositions

Whole-rock compositions of the diorite and granodiorite samples were analyzed at the Beijing Nuclear Industry Geological Analysis and Test Center. Major element analysis was conducted using a Philips PW2404 XRF with testing precision greater than 1%. Trace element analysis was performed using a Finnigan MAT Element I ICP-MS, with RSD (10 min) <1% and RSD (4 h) <5%. For the testing methods, please refer to Gao et al. (2002).

3.2.3. Hf isotopic analyses

In situ zircon Hf isotopic analyses were measured using a Neptune MC-ICP-MS, equipped with a Geolas 193 nm laser-ablation system at the Institute of Geology and Geophysics, Chinese Academy of Science in Beijing. Depending on the zircon size, a stationary beam spot with spot size of approximately 60 μm was employed for the analyses, and the international standard zircon sample GJ-1 was used as a reference. Raw count rates for ^{172}Yb , ^{173}Yb , ^{175}Yb , ^{176}Lu , $^{176}(\text{Hf} + \text{Yb} + \text{Lu})$, ^{177}Hf , ^{178}Hf , ^{179}Hf , ^{180}Hf and ^{182}W were collected and isobaric interference corrections for ^{176}Lu and ^{176}Yb on ^{176}Hf must be determined precisely. Details on the instrumental conditions and data acquisition are given in Wu et al. (2006a). The measured values of the well-characterized zircon standard (GJ-1) agreed with the recommended

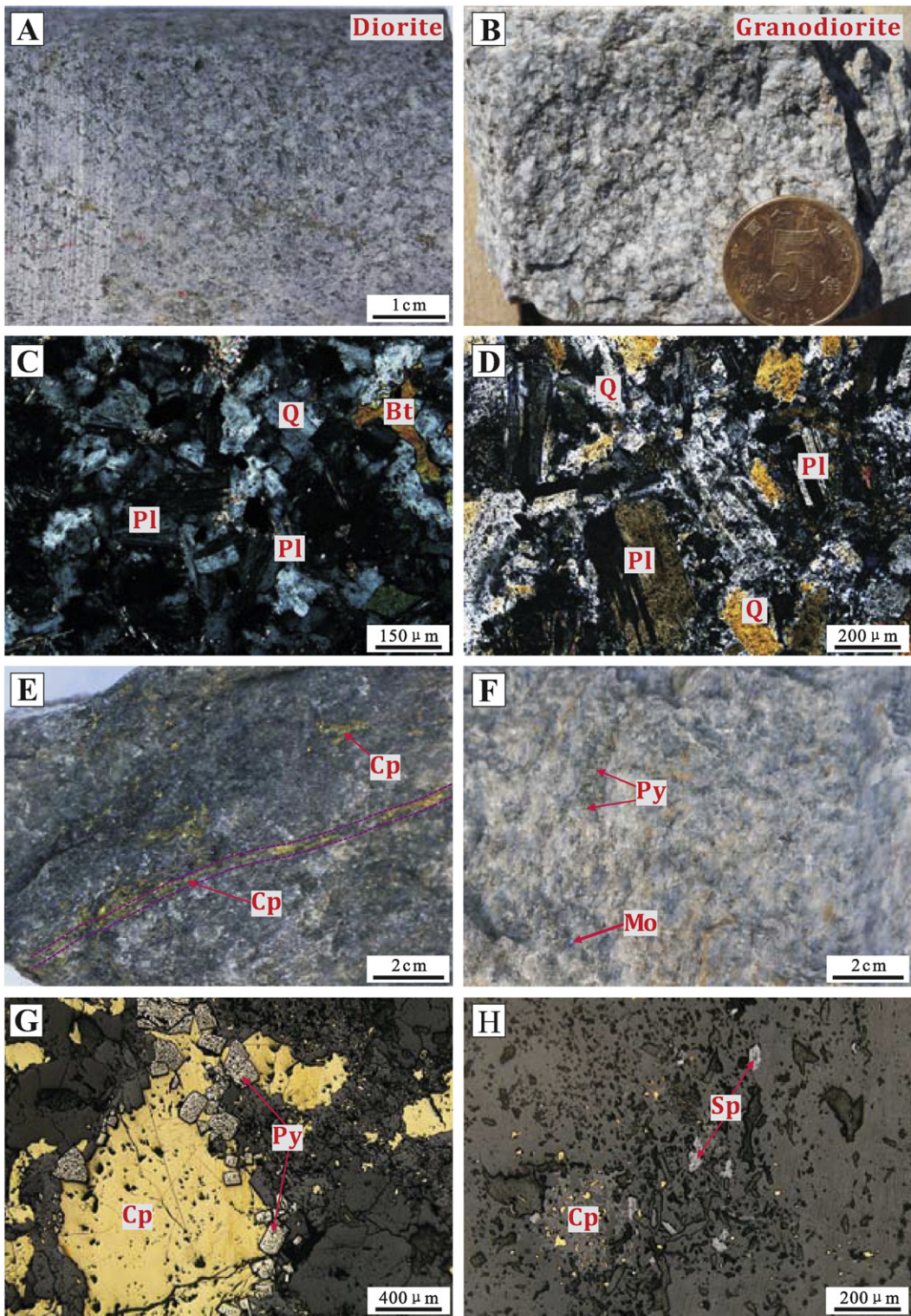


Fig. 4. Photographs and photomicrographs showing the mineralogy of intrusions and mineralization features of the Yuhai porphyry Cu-Mo deposit. (A) Hand specimen of diorite; (B) hand specimen of granodiorite; (C) photomicrograph of diorite, showing plagioclase, quartz and biotite, under crossed-polarized light; (D) photomicrograph of granodiorite, showing hypidiomorphic-xenomorphic plagioclase and quartz, under crossed-polarized light; (E) fine-grained chalcopyrite vein and scattered chalcopyrite in altered diorite; (F) disseminated pyrite and molybdenite in altered granodiorite; (G) anhedral chalcopyrite and euhedral–subhedral pyrite assemblages, under reflected light; (H) sulphides assemblage showing anhedral chalcopyrite and sphalerite, under reflected light. Abbreviations: Q – quartz; Bt – biotite; Pl – plagioclase; Cp – chalcopyrite; Py – Pyrite; Mo – molybdenite; Sp – sphalerite.

values to within 2σ . The weighted average of the $^{176}\text{Hf}/^{177}\text{Hf}$ ratio of the GJ-1 zircon samples was 0.282006 ± 0.000006 (2σ , $n = 71$), consistent with the recommended values (Elhlou et al., 2006) to within 2σ . The initial $^{176}\text{Lu}/^{177}\text{Hf}$ ratios were calculated by using a decay constant of $1.867 \times 10^{-11} \text{ year}^{-1}$ for ^{176}Lu (Soderlund et al., 2004). The chondritic

values of the $^{176}\text{Lu}/^{177}\text{Hf}$ ratio of 0.0332 and $^{176}\text{Hf}/^{177}\text{Hf}$ ratio of 0.282772 (Blichert-Toft and Albarède, 1997) were adopted to calculate the $\epsilon_{\text{Hf}}(t)$ values. The T_{DM} (depleted mantle model age) was measured in reference to the depleted mantle at a present-day $^{176}\text{Lu}/^{177}\text{Hf}$ ratio of 0.0384 and $^{176}\text{Hf}/^{177}\text{Hf}$ ratio of 0.28325 (Griffin et al., 2002). The

Table 1

LA-ICP-MS zircon U-Pb data for the Yuhai diorite and granodiorite in eastern Tianshan.

Spot	Element (ppm)			Th/U	Isotope ratio						Apparent age (Ma)					
	Pb*	U	Th		$^{207}\text{Pb}/^{206}\text{Pb}$	1σ	$^{207}\text{Pb}/^{235}\text{U}$	1σ	$^{206}\text{Pb}/^{238}\text{U}$	±1σ	$^{207}\text{Pb}/^{206}\text{Pb}$	1σ	$^{207}\text{Pb}/^{235}\text{U}$	1σ	$^{206}\text{Pb}/^{238}\text{U}$	1σ
<i>14YH-2, diorite, 24 spots (without spot 06), weighted mean age = 441.6 ± 2.5 Ma, MSWD = 0.03</i>																
01	12	172	67	0.39	0.05571	0.00158	0.54355	0.01509	0.07074	0.00096	441	38	441	10	441	6
02	7	97	29	0.30	0.05595	0.00211	0.54675	0.02019	0.07086	0.00103	450	56	443	13	441	6
03	11	149	63	0.42	0.05572	0.00176	0.54473	0.01699	0.07089	0.00095	441	46	442	11	442	6
04	7	102	28	0.28	0.05581	0.00241	0.55042	0.02322	0.07151	0.00110	445	66	445	15	445	7
05	15	213	95	0.45	0.05544	0.00168	0.54232	0.01624	0.07093	0.00094	430	43	440	11	442	6
06	16	226	105	0.46	0.05536	0.00177	0.52798	0.01662	0.06916	0.00093	427	46	430	11	431	6
07	12	167	63	0.38	0.05574	0.00183	0.54456	0.01762	0.07084	0.00095	442	48	441	12	441	6
08	8	117	42	0.35	0.05624	0.00235	0.55054	0.02275	0.07098	0.00098	462	67	445	15	442	6
09	6	83	26	0.32	0.05581	0.00231	0.54582	0.02223	0.07091	0.00104	445	64	442	15	442	6
10	10	146	41	0.28	0.05533	0.00203	0.54112	0.01958	0.07091	0.00095	426	57	439	13	442	6
11	12	167	64	0.38	0.05595	0.00171	0.54531	0.01634	0.07067	0.00095	450	43	442	11	440	6
12	7	99	34	0.34	0.05573	0.00324	0.54316	0.03101	0.07067	0.00119	442	97	441	20	440	7
13	10	145	61	0.42	0.05553	0.00204	0.54294	0.01965	0.07089	0.00097	434	56	440	13	442	6
14	12	178	54	0.30	0.05571	0.00155	0.54503	0.01488	0.07093	0.00093	441	38	442	10	442	6
15	8	110	35	0.32	0.05558	0.00207	0.54138	0.01979	0.07063	0.00100	436	56	439	13	440	6
16	3	43	11	0.25	0.05561	0.00499	0.54458	0.04809	0.07100	0.00145	437	162	441	32	442	9
17	8	119	35	0.30	0.05564	0.00215	0.54436	0.02055	0.07093	0.00104	438	58	441	14	442	6
18	3	48	15	0.31	0.05562	0.00507	0.54439	0.04915	0.07096	0.00129	437	170	441	32	442	8
19	8	110	39	0.35	0.05597	0.00284	0.54757	0.02732	0.07093	0.00109	451	83	443	18	442	7
20	9	126	49	0.39	0.05553	0.00189	0.54269	0.01806	0.07086	0.00101	434	49	440	12	441	6
21	7	102	48	0.47	0.05551	0.00255	0.54100	0.02442	0.07067	0.00105	433	74	439	16	440	6
22	12	171	70	0.41	0.05555	0.00213	0.54204	0.02044	0.07074	0.00100	434	59	440	13	441	6
23	12	167	61	0.36	0.05577	0.00287	0.54758	0.02791	0.07118	0.00103	443	88	443	18	443	6
24	7	94	37	0.39	0.05561	0.00320	0.54516	0.03088	0.07108	0.00115	437	97	442	20	443	7
25	6	78	41	0.53	0.05573	0.00337	0.54713	0.03255	0.07118	0.00116	442	104	443	21	443	7
<i>14YH-01, granodiorite, 19 spots (without spots 01, 12, 13, 14, 23, and 24), weighted mean age = 430.4 ± 2.9 Ma, MSWD = 0.04</i>																
01	8	68	27	0.40	0.19030	0.00503	0.207942	0.05192	0.07924	0.00118	2745	22	1142	17	492	7
02	5	62	27	0.43	0.05542	0.00263	0.52659	0.02456	0.06890	0.00102	429	77	430	16	430	6
03	7	99	51	0.51	0.05523	0.00205	0.52608	0.01910	0.06908	0.00097	422	56	429	13	431	6
04	9	122	62	0.51	0.05558	0.00249	0.53094	0.02351	0.06927	0.00097	436	74	432	16	432	6
05	3	47	20	0.42	0.05557	0.00365	0.53088	0.03419	0.06927	0.00123	435	112	432	23	432	7
06	7	103	34	0.33	0.05833	0.00259	0.55729	0.02440	0.06928	0.00097	542	71	450	16	432	6
07	7	91	33	0.36	0.05580	0.00245	0.53174	0.02293	0.06911	0.00101	444	70	433	15	431	6
08	6	83	19	0.23	0.05568	0.00288	0.53067	0.02700	0.06912	0.00106	440	86	432	18	431	6
09	7	95	27	0.29	0.05550	0.00332	0.52764	0.03115	0.06894	0.00107	432	104	430	21	430	6
10	4	60	16	0.26	0.05505	0.00470	0.52020	0.04392	0.06853	0.00123	414	158	425	29	427	7
11	10	132	52	0.40	0.05550	0.00287	0.52811	0.02687	0.06900	0.00103	432	87	431	18	430	6
12	12	138	40	0.29	0.06516	0.00588	0.56140	0.04974	0.06249	0.00105	779	197	452	32	391	6
13	12	122	47	0.39	0.06009	0.00577	0.60683	0.05738	0.07325	0.00125	607	216	482	36	456	8
14	5	60	18	0.30	0.05721	0.00934	0.56311	0.09144	0.07137	0.00150	500	324	454	59	444	9
15	7	101	28	0.28	0.05536	0.00477	0.52606	0.04501	0.06891	0.00112	427	164	429	30	430	7
16	12	156	71	0.46	0.05565	0.00268	0.52889	0.02512	0.06891	0.00101	438	80	431	17	430	6
17	7	93	25	0.27	0.05545	0.00566	0.52765	0.05341	0.06900	0.00123	430	196	430	36	430	7
18	4	54	13	0.25	0.05598	0.00593	0.52913	0.05517	0.06854	0.00155	452	194	431	37	427	9
19	5	72	18	0.25	0.05591	0.00357	0.52914	0.03313	0.06863	0.00124	449	107	431	22	428	7
20	7	104	32	0.31	0.05535	0.00390	0.52828	0.03673	0.06921	0.00117	426	126	431	24	431	7
21	5	75	30	0.40	0.05552	0.00493	0.52931	0.04649	0.06914	0.00123	433	166	431	31	431	7
22	7	94	39	0.41	0.05521	0.00440	0.52599	0.04147	0.06909	0.00115	421	148	429	28	431	7
23	6	60	16	0.27	0.13934	0.00885	1.53544	0.09441	0.07991	0.00165	2219	78	945	38	496	10
24	11	141	48	0.34	0.07438	0.00329	0.74967	0.03259	0.07309	0.00108	1052	64	568	19	455	6
25	8	110	32	0.29	0.05525	0.00348	0.52571	0.03252	0.06899	0.00121	422	107	429	22	430	7
<i>14YH-02, granodiorite, 24 spots (without spot 09), weighted mean age = 430.3 ± 2.6 Ma, MSWD = 0.09</i>																
01	9	123	43	0.35	0.05536	0.00270	0.52885	0.02530	0.06926	0.00104	427	80	431	17	432	6
02	6	83	22	0.27	0.05579	0.00310	0.53224	0.02916	0.06916	0.00105	444	95	433	19	431	6
03	6	87	37	0.42	0.05529	0.00220	0.52781	0.02045	0.06921	0.00105	424	59	430	14	431	6
04	8	112	42	0.37	0.05559	0.00202	0.52808	0.01877	0.06887	0.00095	436	54	431	12	429	6
05	4	50	16	0.32	0.05560	0.00312	0.53148	0.02914	0.06931	0.00117	436	92	433	19	432	7
06	8	110	48	0.44	0.05918	0.00250	0.56475	0.02346	0.06919	0.00099	574	65	455	15	431	6
07	5	72	19	0.26	0.05532	0.00256	0.52840	0.02391	0.06926	0.00106	425	73	431	16	432	6
08	5	79	20	0.26	0.05523	0.00332	0.51723	0.03063	0.06790	0.00107	422	104	423	20	423	6
09	4	54	19	0.35	0.05602	0.00360	0.55040	0.03468	0.07124	0.00123	453	109	445	23	444	7
10	6	85	23	0.27	0.05527	0.00298	0.52632	0.02789	0.06905	0.00108	423	90	429	19	430	7
11	6	88	27	0.31	0.05537	0.00225	0.52655	0.02090	0.06895	0.00102	427	62	430	14	430	6
12	8	119	32	0.27	0.05539	0.00249	0.									

Table 1 (continued)

Spot	Element (ppm)			Th/U	Isotope ratio						Apparent age (Ma)									
	Pb*	U	Th		$^{207}\text{Pb}/^{206}\text{Pb}$		1σ	$^{207}\text{Pb}/^{235}\text{U}$		1σ	$^{206}\text{Pb}/^{238}\text{U}$		±1σ	$^{207}\text{Pb}/^{206}\text{Pb}$		1σ	$^{207}\text{Pb}/^{235}\text{U}$		1σ	$^{206}\text{Pb}/^{238}\text{U}$
19	8	106	31	0.29	0.05553	0.00381	0.52751	0.03562	0.06888	0.00118	434	120	430	24	429	7				
20	4	61	17	0.28	0.05546	0.00487	0.52779	0.04563	0.06901	0.00134	431	160	430	30	430	8				
21	7	96	29	0.30	0.05539	0.00358	0.52683	0.03339	0.06897	0.00118	428	111	430	22	430	7				
22	4	58	18	0.31	0.05554	0.00693	0.53026	0.06565	0.06922	0.00138	434	243	432	44	431	8				
23	11	150	71	0.48	0.05554	0.00251	0.52964	0.02341	0.06915	0.00103	434	72	432	16	431	6				
24	8	104	30	0.29	0.05577	0.00405	0.52919	0.03775	0.06880	0.00127	443	126	431	25	429	8				
25	7	92	42	0.46	0.05533	0.00326	0.52979	0.03050	0.06943	0.00118	426	98	432	20	433	7				

T_{DM}^{c} (crustal model age) was calculated using an average continental crustal $^{176}\text{Lu}/^{177}\text{Hf}$ ratio of 0.015 (Griffin et al., 2002).

3.2.4. Re–Os isotopic analyses

Molybdenite was magnetically separated and then handpicked under a binocular microscope. Sample preparation and mineral separation followed techniques outlined by Shirey and Walker (1995), Mao

et al. (1999), and Du et al. (2004). Re–Os isotopic analyses were carried out at the Re–Os Laboratory of National Research Center of Geoanalysis, Chinese Academy of Geological Sciences, Beijing. Re–Os isotopic data were obtained by isotope dilution ICP–MS (TJA X-series ICP–MS). The decay constant used in the age calculation was $\lambda^{187}\text{Re} = 1.666 \times 10^{-11} \text{ year}^{-1}$ (Smoliar et al., 1996). Uncertainty in Re–Os model ages includes 1.02% uncertainty in the ^{187}Re decay constant and uncertainty

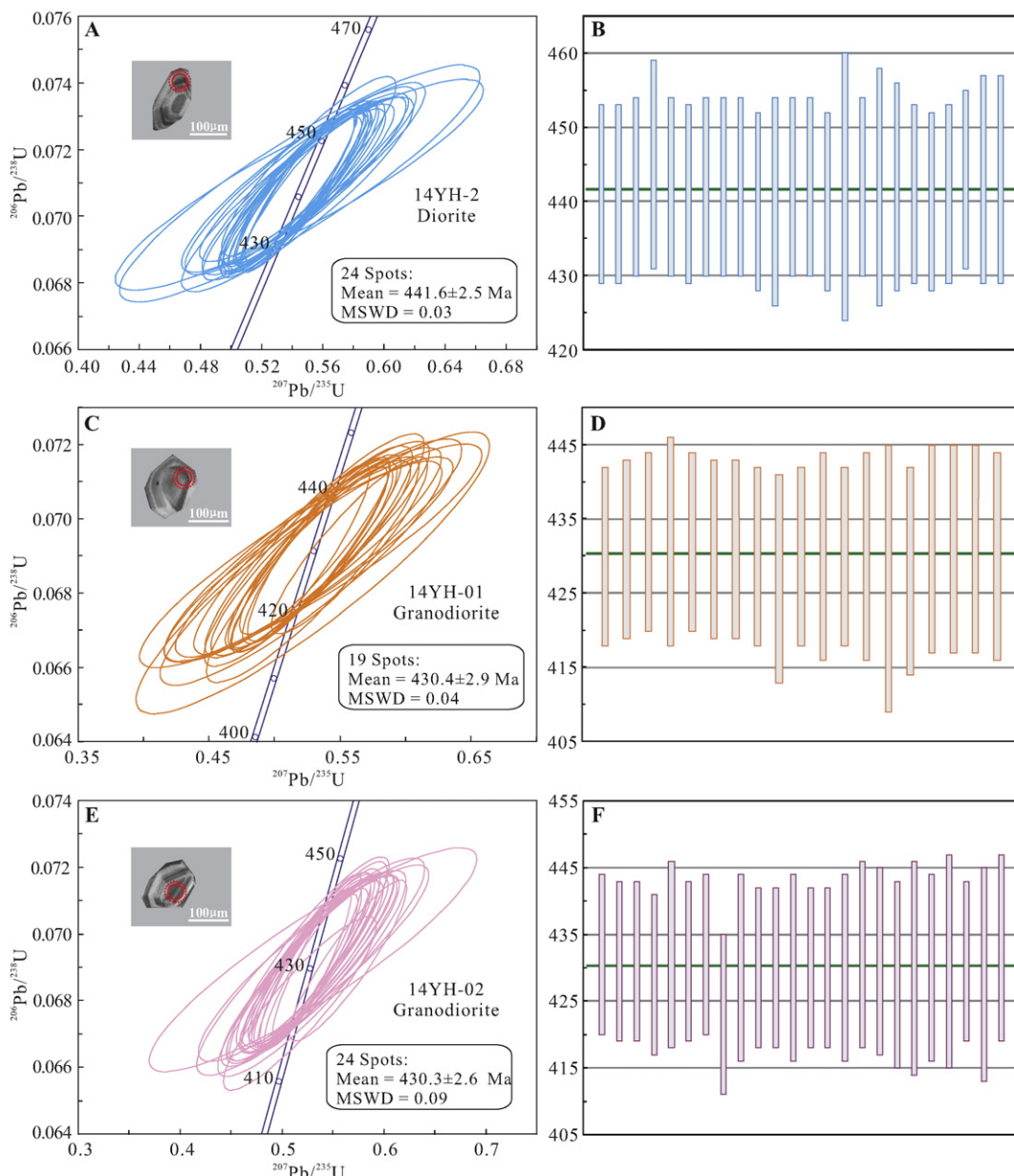


Fig. 5. Cathodoluminescence images, concordia and weighted diagrams of the zircon U–Pb age of the diorite (A and B) and granodiorite (C, D, E and F) in the Yuhai porphyry Cu–Mo deposit.

Table 2

Zircon trace element data for the Yuhai diorite and granodiorite in eastern Tianshan.

Chondrite REE values are after Sun and McDonough (1989).

Spot	Ti	Y	La	Ce	Pr	Nd	Sm	Eu	Gd	Tb	Dy	Ho	Er	Tm	Yb	Lu	Hf	Th	U	Pb	Th/U	(La/Yb)chn	Eu/Eu*	Ce/Ce*	T
<i>14YH-2, diorite</i>																									
01	7.31	1124	0.057	22.4	0.095	1.48	3.42	1.6	17.35	7.04	91.67	38.96	190.9	54.4	690.4	161.78	7910	67	172	12.1	0.39	0.00006	0.64	74.63	714
02	7.11	757.1	0.051	12.12	0.048	1.02	2.24	1.151	11.68	4.42	60.26	26.56	137	39.35	519.7	127.40	7613	29	97	6.7	0.30	0.00007	0.69	60.06	712
03	7.1	1196	0.076	18.86	0.17	3.04	5.56	2.38	22.53	8.11	103.5	42.89	209.1	57.93	726.6	174.68	7500	63	149	10.6	0.42	0.00008	0.65	40.68	712
04	6.91	760.8	0.066	12.32	0.069	1.2	2.14	1.268	11.45	4.48	60.99	26.89	141.3	40.62	532.8	136.49	7730	28	102	7.0	0.28	0.00009	0.78	44.76	709
05	7.79	1390	0.083	25.86	0.116	2.89	5.11	2.32	24.96	9.54	119.3	48.99	239.5	65.93	821.3	191.95	7979	95	213	15.3	0.45	0.00007	0.63	64.62	719
06	10.1	1386	0.108	27.54	0.086	1.77	4.32	2.09	23.96	9.13	119.3	49.48	243.5	67.6	862.9	201.43	7621	105	226	15.9	0.46	0.00009	0.63	70.06	741
07	9.16	1166	0.067	19.88	0.083	1.74	3.16	1.66	16.56	6.77	93.08	40.97	207.2	58.98	759.3	188.67	8449	63	167	11.8	0.38	0.00006	0.70	65.36	733
08	6.33	796.2	0.082	15.09	0.058	1.11	2.28	1.236	12.8	5.19	68.83	29.18	146.3	42.23	547.6	128.79	7720	42	117	8.3	0.35	0.00011	0.70	53.65	702
09	6.78	569.5	7.56	23.49	1.93	8.69	3.43	1.217	10.13	3.68	46.96	19.82	100.7	28.7	381.5	90.25	7007	26	83	5.8	0.32	0.01422	0.63	1.51	708
10	7.76	876.4	0.278	17.08	0.426	5.07	4.42	1.54	14.27	5.16	68.99	30.11	157.1	45.65	613.2	147.83	7329	41	146	10.1	0.28	0.00033	0.59	12.17	719
11	8.45	1130	0.061	20.48	0.07	1.54	3.15	1.53	17.39	6.98	94.82	39.81	199.7	56.32	735	168.49	7226	64	167	11.9	0.38	0.00006	0.63	76.84	726
12	6.43	865	0.124	12.25	0.17	2.69	5.13	1.67	20.64	6.71	77.33	28.78	137.8	37.71	473	114.91	7164	34	99	6.9	0.34	0.00019	0.50	20.69	703
13	8.54	1091	0.067	19.8	0.091	1.07	2.6	1.7	18.16	7.16	92.6	38.79	188.7	52.62	681.3	155.79	7004	61	145	10.4	0.42	0.00007	0.76	62.17	727
14	7.87	1034	0.076	18.72	0.059	1.42	3.15	1.47	14.66	5.67	80.84	36.55	189.6	55.43	733.1	171.97	7358	54	178	12.5	0.30	0.00007	0.66	68.54	720
15	7.18	658.5	0.074	12.2	0.05	0.8	2.27	0.953	9.85	3.76	51.05	22.19	111.6	32.6	434.5	104.04	7189	35	110	7.7	0.32	0.00012	0.62	49.17	713
16	4.77	364.6	0.089	5.63	0.069	0.56	1.54	0.613	5.94	2.21	28.26	11.84	59.13	17.32	241.9	57.03	8187	11	43	3.0	0.25	0.00026	0.62	17.61	680
17	6.56	759.1	0.085	13.71	0.05	1.17	2.4	1.184	11.29	4.22	58.97	25.85	132.7	39.23	542.2	126.16	7526	35	119	8.4	0.30	0.00011	0.70	51.56	705
18	5.3	418.5	0.113	6.08	0.063	0.91	1.61	0.718	6.87	2.76	33.77	13.16	64.33	18.34	247.4	59.60	7420	15	48	3.4	0.31	0.00033	0.66	17.67	688
19	6.57	771.4	0.119	12.72	0.073	0.77	1.97	1.116	12.08	4.4	59.35	25.43	125.7	34.98	472.2	114.22	7337	39	110	7.9	0.35	0.00018	0.70	33.46	705
20	6.98	902.3	0.062	14.01	0.091	1.81	3.44	1.77	17.19	6.33	79.39	32.66	161.3	45.98	596.5	140.80	6935	49	126	9.1	0.39	0.00007	0.70	45.73	710
21	5.3	641.7	0.091	9.19	0.075	2.16	3.91	1.63	15.01	4.79	56.81	20.99	97.14	26.8	344.2	77.00	8632	48	102	7.4	0.47	0.00019	0.65	27.27	688
22	8.19	1243	0.109	21.92	0.108	1.81	4.05	2.03	20.75	8	105	44.99	219.1	61.53	784.4	180.42	7087	70	171	12.4	0.41	0.00010	0.68	49.53	724
23	11.1	1128	0.145	20.51	0.091	1.17	3.24	1.76	17.93	7	95.14	40.07	199.4	57.15	748.5	171.55	7433	61	167	12.0	0.36	0.00014	0.71	43.78	750
24	5.46	490.6	0.113	11.25	0.08	0.66	1.42	0.898	7.63	3.06	39.67	16.33	78.73	22.43	294.4	68.70	7923	37	94	6.9	0.39	0.00028	0.83	29.01	690
25	8.12	992.8	0.076	12.53	0.173	3.4	6.86	2.19	26.65	8.72	100.7	37.39	168.3	43.84	507.6	104.86	7591	41	78	5.8	0.53	0.00011	0.50	26.79	723
<i>14YH-01, granodiorite</i>																									
01	6.01	728.8	0.065	9.33	0.154	2.31	3.85	1.83	16.74	5.69	67.68	25.61	123.8	33.45	423.1	102.75	7857	27	68	7.9	0.40	0.00011	0.70	22.86	698
02	5.47	704.1	0.055	8.79	0.137	2.59	5.43	2.23	18.97	6.19	70.34	25.78	119.5	31.53	389.4	89.35	7549	27	62	4.6	0.43	0.00010	0.67	24.83	690
03	8.45	888.3	0.046	14.35	0.225	3.82	6.78	2.04	24.04	7.73	88.7	33.11	147.3	36.95	438.2	93.02	8046	51	99	7.4	0.51	0.00008	0.49	34.58	726
04	6.12	1118	0.059	15.42	0.26	3.72	7.13	3.21	31.05	9.84	112.6	41.37	188.3	49.5	615.4	142.61	7214	62	122	9.2	0.51	0.00007	0.66	30.53	699
05	8.94	540	0.063	11.19	0.068	0.86	3.15	0.904	12.72	4.39	52.59	18.42	82.29	21.22	251.4	50.62	8259	20	47	3.5	0.42	0.00018	0.44	41.92	731
06	7.98	742.2	0.079	11.63	0.056	1.22	2.3	1.166	10.96	4.58	62.08	26.97	139.6	39.1	515.2	119.51	7201	34	103	7.5	0.33	0.00011	0.71	42.87	721
07	6.16	803.4	0.069	11.49	0.131	2.4	4.47	2.22	18.79	6.18	76.93	29.45	139.4	38.57	491.1	111.77	7369	33	91	6.6	0.36	0.00010	0.74	29.63	700
08	6.84	676.9	0.079	9.15	0.066	0.87	2.32	1.015	9.57	3.51	48.18	20.72	111.1	32.36	454.6	109.32	7590	19	83	5.8	0.23	0.00012	0.66	31.07	709
09	6.13	701.5	0.107	12.39	0.091	0.99	2.03	1.063	10.51	4.06	55.65	23.79	120.3	34.84	459.5	110.62	8111	27	95	6.8	0.29	0.00017	0.70	30.79	700
10	8.37	546.2	0.107	8.38	0.071	0.81	2.05	0.898	8.32	3.23	42.41	17.94	90.33	25.35	344	82.71	7912	16	60	4.2	0.26	0.00022	0.66	23.57	725
11	6.69	1158	0.087	17.05	0.172	3.47	6.82	2.52	24.32	8.6	108	42.41	203.8	55.6	709.9	162.66	7837	52	132	9.6	0.40	0.00009	0.60	34.17	707

(continued on next page)

Table 2 (continued)

Spot	Ti	Y	La	Ce	Pr	Nd	Sm	Eu	Gd	Tb	Dy	Ho	Er	Tm	Yb	Lu	Hf	Th	U	Pb	Th/U	(La/Yb)chn	Eu/Eu*	Ce/Ce*	T
12	7.84	923.2	0.196	14.84	0.127	2.12	3.13	1.33	14.47	5.32	72.31	30.29	154.2	43.02	568.6	132.56	7328	40	138	12.3	0.29	0.00025	0.60	23.06	720
13	7.59	1056	0.212	15.39	0.135	2.32	4.45	1.92	20.09	7.04	89.15	36	169.2	46.22	604	140.24	7364	47	122	11.9	0.39	0.00025	0.62	22.30	717
14	8.82	358.6	0.252	7.6	0.165	1.19	1.58	0.53	5.76	1.9	27.66	11.41	58.63	17.05	225.7	54.45	7672	18	60	4.6	0.30	0.00080	0.54	9.14	730
15	6.57	766.4	0.151	12.31	0.096	1.37	2.41	1.185	11.09	4.27	56.98	24.5	126.7	36.02	490.6	114.59	7500	28	101	7.0	0.28	0.00022	0.70	25.07	705
16	8.07	1136	0.078	20.67	0.097	1.29	3.51	1.81	20.56	7.75	98.62	38.79	188.9	51.84	654.3	150.38	7082	71	156	11.5	0.46	0.00009	0.65	58.26	722
17	4.99	668.5	0.184	9.76	0.112	0.93	2.41	1.35	11.62	3.96	53.94	21.43	108.8	30.78	413.9	99.85	7518	25	93	6.6	0.27	0.00032	0.78	16.67	683
18	16.8	467.2	0.123	6.35	0.068	0.9	0.87	0.863	7.39	2.89	37.73	15.16	79.11	22.14	312	74.28	7106	13	54	3.9	0.25	0.00028	1.04	17.02	789
19	6.57	671.7	0.069	9.64	0.047	1.03	1.8	1.022	9.88	3.59	51.06	21.65	111.3	31.98	427.6	102.57	6999	18	72	5.0	0.25	0.00012	0.74	41.50	705
20	5.8	452.1	0.131	10.54	0.119	1.06	1.82	0.806	7.36	2.76	34.84	14.81	73.85	21.4	294.3	70.83	8005	32	104	7.5	0.31	0.00032	0.67	20.70	695
21	4.8	789.4	0.179	9.5	0.17	2.89	4.34	2.23	18.43	6.31	72.08	27.17	124.5	33.86	437.7	95.08	7513	30	75	5.5	0.40	0.00029	0.76	13.35	680
22	6.01	890.3	0.159	11.89	0.136	2.83	5.59	2.47	20.71	6.7	78.49	29.8	137.4	37.06	489.1	108.53	7047	39	94	7.0	0.41	0.00023	0.70	19.82	698
23	7.55	495.8	0.139	8.24	0.126	0.9	1.24	0.955	7.19	2.7	38.02	15.51	79.28	22.55	308.2	71.95	7080	16	60	6.5	0.27	0.00032	0.98	15.27	717
24	9.28	1147	0.146	18.83	0.104	1.36	2.65	1.43	17.28	6.84	92.99	39.47	197.3	55.05	718.6	161.70	6700	48	141	11.5	0.34	0.00015	0.65	37.47	734
25	7.6	846	0.098	13.14	0.081	0.84	2.75	1.18	11.84	4.98	66.56	28.5	139.6	41.14	547.5	126.25	7153	32	110	7.8	0.29	0.00013	0.63	36.16	717
<i>14YH-02, granodiorite</i>																									
01	6.26	744.1	0.076	14.4	0.081	1.04	2.83	1.13	12.84	4.48	61.97	26.22	134.2	38.75	505.8	122.55	8287	43	123	8.9	0.35	0.00011	0.57	45.00	701
02	6.25	597.2	0.064	10.24	0.056	0.91	1.86	0.951	10.18	3.79	50.3	21.54	109.4	32.72	436.7	104.73	8047	22	83	5.9	0.27	0.00011	0.67	41.94	701
03	9.66	931.4	0.041	14.36	0.125	2.55	5.23	1.72	21.16	7.56	90.84	34.79	164.2	43.08	519.5	114.42	7712	37	87	6.3	0.42	0.00006	0.50	49.18	738
04	6.01	928.5	0.043	13.82	0.104	1.63	4.08	1.91	18.63	6.47	83.59	33.48	167	46.88	610.7	146.33	7120	42	112	8.1	0.37	0.00005	0.67	50.67	698
05	6.19	404.4	0.042	6.65	0.033	0.638	1.21	0.57	6.45	2.38	31.34	13.02	66.62	19.34	263	63.81	7991	16	50	3.6	0.32	0.00011	0.62	43.80	700
06	5.79	1038	0.088	14.85	0.229	4.12	6.4	2.75	25.85	8.8	101.8	39.73	183.7	49.16	613.9	141.69	7670	48	110	8.2	0.44	0.00010	0.65	25.65	695
07	6.35	525.9	0.054	8.83	0.047	0.52	1.7	0.865	8.68	3.1	40.51	17.71	92.22	26.58	360.8	86.32	7656	19	72	5.1	0.26	0.00011	0.69	42.97	702
08	6.54	588.1	0.087	9.25	0.074	1.05	2.02	0.895	9.74	3.43	46.05	19.73	103.5	30.57	410.4	100.18	7590	20	79	5.5	0.26	0.00015	0.62	28.27	705
09	5.74	529.3	0.076	7.45	0.106	1.57	2.96	1.4	12.05	4.08	48.5	18.23	88.3	24.46	318.4	73.95	7448	19	54	4.1	0.35	0.00017	0.72	20.35	694
10	6.92	642.2	0.074	10.84	0.058	0.88	2.04	1.07	10.71	3.91	53.01	22.37	118.5	33.78	456	109.33	7666	23	85	6.0	0.27	0.00012	0.70	40.57	709
11	6.24	703.3	0.044	11.04	0.04	1.13	2.83	1.26	12.72	4.74	62.66	25.26	125.4	35.25	463	108.13	6672	27	88	6.3	0.31	0.00007	0.64	64.52	701
12	6.22	710.1	0.113	12.32	0.067	0.8	2.24	1.17	10.79	4.31	56.84	24.71	125.9	36.8	490.1	117.19	7765	32	119	8.4	0.27	0.00017	0.73	34.72	701
13	5.58	560	0.085	8.38	0.047	0.83	1.66	0.909	8.74	3.21	42.07	18.05	92.52	27.19	357.5	87.46	7218	19	63	4.5	0.30	0.00017	0.73	32.51	692
14	10.5	1665	0.066	30.43	0.072	2.05	4.43	2.7	31.19	11.67	154.2	60.27	293	78.76	1022	226.42	7266	100	222	16.5	0.45	0.00005	0.70	108.23	745
15	8.93	1091	0.092	19.77	0.098	1.33	2.99	1.67	18.6	7.25	93.94	38.22	184.7	51.12	644.8	147.16	7422	61	144	10.5	0.42	0.00010	0.68	51.05	731
16	7.6	633.1	0.114	8.95	0.056	0.82	1.77	0.933	9.04	3.41	45.46	20.26	105.4	30.86	422.8	101.41	7226	18	78	5.5	0.23	0.00019	0.71	27.46	717
17	7.46	1041	0.074	17.04	0.202	3.04	5.33	2.24	21.67	7.29	91.85	38.1	182.8	52.42	674.7	150.21	7397	50	142	10.4	0.35	0.00008	0.64	34.17	716
18	6.55	711.6	0.135	10.44	0.085	0.78	2.28	0.85	10.08	3.79	54.66	22.7	119.4	34.98	482.4	115.48	7514	20	88	6.2	0.23	0.00020	0.54	23.90	705
19	7.68	869.9	0.104	13.29	0.083	1.23	2.5	1.23	12.39	4.91	66.66	28.26	148.1	41.5	566.7	133.40	7132	31	106	7.7	0.29	0.00013	0.68	35.07	718
20	6.9	391.8	0.088	7.59	0.07	0.5	1.18	0.633	5.93	2.35	29.84	12.66	63.02	17.9	244.5	57.28	7765	17	61	4.4	0.28	0.00026	0.73	23.71	709
21	8.45	729.6	0.114	11.34	0.087	1.1	2.93	1.4	12.62	4.47	57.54	23.15	113.4	32.5	423.4	97.90	6925	29	96	6.9	0.30	0.00019	0.70	27.92	726
22	6.31	569.5	0.233	7.69	0.102	1.23	2.45	1.53	11.13	3.92	48.25	18.67	90.11	25.03	325.1	73.96	7143	18	58	4.3	0.31	0.00051	0.90	12.23	702
23	4.42	506.5	0.069	9.24	0.077	1.92	3.33	1.4	10.56	3.43	40.62	15.76	78.98	23.45	319.4	77.24	9126	71	150	11.3	0.48	0.00015	0.72	31.08	674
24	6.39	804.2	0.148	12.14	0.082	0.87	2.15	0.99	11.31	4.55	61.03	26.29	132.2	36.85	509.5	120.58	7733	30	104	7.5	0.29	0.00021	0.61	27.02	703
25	6.99	771.6	0.073	11.58	0.193	3.04	5.35	1.69	18.85	5.88	67.89	25.84	118.1	31.47	392.9	83.65	7876	42	92	7.0	0.46	0.00013	0.51	23.92	710

(La/Yb)_N are chondrite normalized ratio; Ce/Ce* = Ce_N/(La_N × Pr_N)^{1/2}; Eu/Eu* = Eu_N/(Sm_N × Gd_N)^{1/2}; Ti-in-zircon temperature T_{Ti} (°C) = 5080 / (6.01 - log Ti_{zircon}) - 273.15 (Watson et al., 2006).

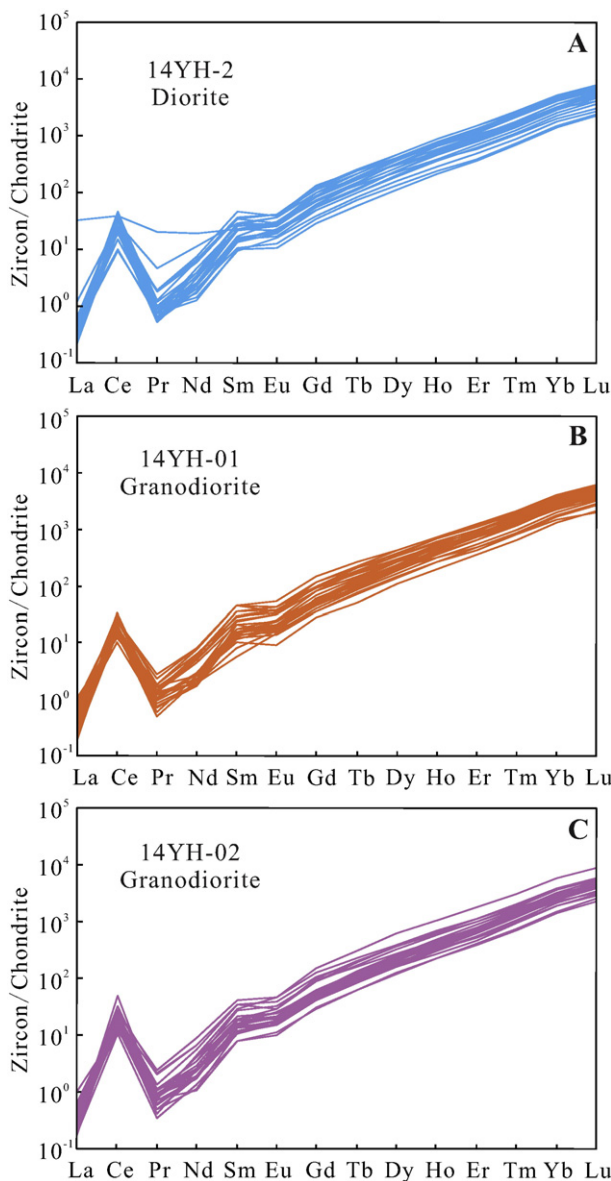


Fig. 6. Chondrite-normalized REE patterns for zircon grains from the Yuhai intrusions. Chondrite values are from Sun and McDonough (1989).

in Re and Os concentrations, which includes weighing error for both spike and sample, uncertainty in spike calibration, and mass spectrometry analytical error.

4. Results

4.1. Zircon U–Pb ages

The Yuhai diorite sample (14YH-2) and granodiorite samples (14YH-01 and 14YH-02) were selected for LA-ICP-MS zircon U–Pb dating, and the analytical data are listed in Table 1. Most of the zircon grains are euhedral–subhedral and show prismatic forms (100–200 μm long) with aspect ratios of 3:2 to 3:1 and exhibit clear oscillatory growth zoning in their CL images (Fig. 5). All of the analyzed zircons have varying U (43–226 ppm) and Th (11–105 ppm) contents, with Th/U ratios ranging from 0.23 to 0.53 (Table 1), which is consistent with a magmatic origin (Hoskin and Schaltegger, 2003). Therefore, the LA-ICP-MS zircon U–Pb dating results are interpreted to represent the timing of zircon

crystallization and thus the age of the magma emplacement. Except for one discordant spot (06), the remaining 24 analyses from the diorite sample (14YH-2) yielded concordant $^{206}\text{Pb}/^{238}\text{U}$ ages varying from 440 to 445 Ma (Fig. 5A), with a weighted mean age of 441.6 ± 2.5 Ma (MSWD = 0.03; n = 24). Except for six discordant spots (01, 12, 13, 14, 23, and 24), the remaining 19 analytical spots from the granodiorite sample (14YH-01) had $^{206}\text{Pb}/^{238}\text{U}$ ages ranging from 427 to 432 Ma (Fig. 5B), with a weighted mean age of 430.4 ± 2.9 Ma (MSWD = 0.04, n = 19). Except for one discordant spot (09), the remaining 24 analytical spots from the granodiorite sample (14YH-02) had $^{206}\text{Pb}/^{238}\text{U}$ ages ranging from 423 to 433 Ma (Fig. 5C), with a weighted mean age of 430.3 ± 2.6 Ma (MSWD = 0.09, n = 24). Thus, we interpret the weighted mean ages as the emplacement ages of the diorite and granodiorite at Yuhai.

4.2. Zircon trace elements

Trace element analyses carried out on zircons from sample 14YH-2 yielded relatively low U (43–226 ppm) and Th (11–105 ppm) contents, with corresponding Th/U ratios of 0.25–0.53 (Table 2). They displayed pronounced LREE depletion with $(\text{La/Yb})_{\text{N}} = 0.00006$ – 0.01422 , positive Ce anomalies with $\text{Ce/Ce}^* = 1.51$ – 76.84 and negative Eu anomalies with $\text{Eu/Eu}^* = 0.50$ – 0.83 (Fig. 6A), similar to those of typical magmatically crystallized zircons (Schaltegger et al., 1999; Hoskin and Ireland, 2000; Hoskin and Schaltegger, 2003; Whitehouse and Platt, 2003). The trace element analyses on zircons from samples 14YH-01 and 14YH-02 had similar U (47–222 ppm) and Th (13–100 ppm) contents and Th/U ratios (0.23–0.51) (Table 2). In addition, these samples had similar chondrite normalized REE patterns with significant HREE enrichments ($(\text{La/Yb})_{\text{N}} = 0.00005$ – 0.00080), and showed strong positive Ce anomalies ($\text{Ce/Ce}^* = 9.14$ – 108.23) and negative Eu anomalies ($\text{Eu/Eu}^* = 0.44$ – 1.04) (Fig. 6B, C). The calculated results of the Ti-in-zircon thermometer can be used to determine the genetic setting of zircons (Fu et al., 2009). The calculated Ti-in-zircon thermometer varied from 680 to 750 °C (avg. 713 °C, n = 25) in the diorite and 680 to 789 °C (avg. 713 °C, n = 25) and 674 to 745 °C (avg. 708 °C, n = 25) in the granodiorite (Table 2). Magmatic zircons crystallize from ore-forming fluids at temperatures higher than 600 °C (Fu et al., 2009; Wan et al., 2012). Therefore, the high formation temperatures and Th/U values of the zircons from the Yuhai deposit can be taken as evidence for their crystallization from magmas, and their Hf isotope compositions can be employed to evaluate their source characteristics.

4.3. Re–Os isotopic ages

The Re–Os isotopic data for four molybdenite samples from the Yuhai porphyry Cu–Mo deposit are listed in Table 3 and are plotted in an isochron diagram in Fig. 7. The concentrations of ^{187}Re and ^{187}Os ranged from 13.5 to 52.2 $\mu\text{g/g}$ and from 79.9 to 307.9 ng/g , respectively. Four samples yielded model ages ranging from 357.9 ± 4.6 to 353.0 ± 5.0 Ma and a well-constrained ^{187}Re – ^{187}Os isochron age of 351.7 ± 2.9 Ma, with MSWD = 1.5 and an initial ^{187}Os of 1.1 ± 0.8 ng/g (Fig. 7A). The data also produced a weighted average age of 355.7 ± 2.4 Ma (MSWD = 0.69) (Fig. 7B). These two ages are concordant within their error limits and indicate that the Yuhai deposit was mineralized in the Carboniferous.

4.4. Whole-rock geochemistry

The representative whole-rock geochemical data for the Yuhai intrusive samples are presented in Table 4, and they plot in the diorite and granodiorite fields on the $\text{Na}_2\text{O} + \text{K}_2\text{O}$ vs. SiO_2 diagram (Fig. 8A; Le Maitre, 2002). The diorite is characterized by high SiO_2 (58.30–62.86 wt.%), Al_2O_3 (15.24–17.36 wt.%) and MgO (1.95–4.80 wt.%) and low $\text{K}_2\text{O} + \text{Na}_2\text{O}$ (3.88–6.32 wt.%), TiO_2 (0.38–0.54 wt.%), P_2O_5 (0.18–0.28 wt.%) and MnO (0.06–0.19 wt.%), which belong to the low-K

Table 3

Molybdenite Re–Os isotopic data for the Yuhai porphyry Cu–Mo deposit.

Sample no.	Weight (g)	Ores type	Occurrence	Re/ $\mu\text{g}\cdot\text{g}^{-1}$		Os/ $\text{ng}\cdot\text{g}^{-1}$		$^{187}\text{Re}/\mu\text{g}\cdot\text{g}^{-1}$		$^{187}\text{Os}/\text{ng}\cdot\text{g}^{-1}$		Model age (Ma)	
				Measured	2σ	Measured	2σ	Measured	2σ	Measured	2σ	Measured	2σ
14YH-13	0.00976	Mo mineralized diorite	Dissemination	83.1	0.69	0.4687	0.0451	52.2	0.43	307.9	1.9	353.0	5.0
14YH-14	0.01048	Mo mineralized granodiorite	Dissemination	22.1	0.13	0.1756	0.0333	13.9	0.08	83.0	0.48	357.9	4.6
14YH-15	0.01013	Ccp-Mo-Qz veinlet	Veinlet	21.4	0.16	0.141	0.0393	13.5	0.1	79.9	0.52	355.6	5.0
14YH-10	0.00525	Ccp-Mo-Qz veinlet	Veinlet	23.0	0.18	0.1945	0.0475	14.5	0.11	85.9	0.5	355.8	4.9

tholeiite series (Fig. 8B). The granodiorite exhibited slightly different major element compositions, having $\text{SiO}_2 = 62.87\text{--}64.32\text{ wt.\%}$, $\text{Al}_2\text{O}_3 = 17.05\text{--}17.39\text{ wt.\%}$, $\text{MgO} = 1.84\text{--}2.55\text{ wt.\%}$ and $\text{Mg}^{\#} = 40\text{--}49[100 \times \text{molar Mg}^{2+}/(\text{Mg}^{2+} + \text{Fe}^{2+})]$; Fig. 8C). These rocks are characterized by low K_2O (0.41–1.33 wt.\%), and $\text{TiFe}_2\text{O}_3/\text{MgO}$ (2.05–3.03), which suggests that they are low-K tholeiite series rocks (Fig. 8B). In the chemical variation diagrams of selected major oxides (Fig. 9), the TiFe_2O_3 , TiO_2 , MnO , MgO and Na_2O contents of all of the intrusive samples correlated negatively with the SiO_2 contents, which suggests possible fractional crystallization during the intrusive process.

In the chondrite-normalized rare earth element (REE) diagram (Fig. 10A; Boynton, 1984), the diorite samples are moderately fractionated ($(\text{La/Yb})_{\text{N}} = 4.19\text{--}7.64$), with light rare earth element (LREE) enrichment and heavy rare earth element (HREE) depletion in the absence of clear Eu anomalies ($\text{Eu/Eu}^* = 0.92\text{--}1.27$). Moreover, the granodiorite samples had slightly different REE patterns ($(\text{La/Yb})_{\text{N}} = 6.40\text{--}19.64$), and the values of the positive Eu anomaly ranged from 1.03 to 1.36 (Fig. 10C). In the primitive mantle-normalized trace element spider diagram (Fig. 10B, D; Sun and McDonough, 1989), both of the diorite and granodiorite samples show an enrichment in U, Pb and large ion lithophile elements (LILEs) such as K, Ba and Sr and a depletion in high field strength elements (HFSEs) such as Th, Nb, Ta and Ti.

4.5. Zircon Hf isotope systematics

In situ Hf isotopic data for zircons from three samples of 14YH-2 (diorite), 14YH-01 and 14YH-02 (granodiorite) are shown in Fig. 11, and the zircon Hf isotopic data and calculation results are presented in Table 5. The magmatic zircons from diorite (441.6 ± 2.5 Ma) exhibited variable Hf isotopic compositions, with $^{176}\text{Hf}/^{177}\text{Hf}$ ratios ranging from 0.282754 to 0.283035. The positive $\epsilon_{\text{Hf}}(t)$ values and Hf isotopic crustal model ages (T_{DM}^{C}) ranged from +8.7 to +18.6 and from 234 to 872 Ma, respectively (Table 5; Fig. 11). The magmatic zircons from granodiorite (430.4 ± 2.9 Ma) had $^{176}\text{Hf}/^{177}\text{Hf}$ ratios varying from 0.282869 to 0.283028, with positive $\epsilon_{\text{Hf}}(t)$ values and corresponding T_{DM}^{C} ages

ranging from +12.6 to +19.6 and from 213 to 612 Ma, respectively (Table 5; Fig. 11). The magmatic zircons from granodiorite (430.3 ± 2.6 Ma) exhibited $^{176}\text{Hf}/^{177}\text{Hf}$ ratios varying from 0.282871 to 0.283052, with positive $\epsilon_{\text{Hf}}(t)$ values and corresponding T_{DM}^{C} ages ranging from +12.6 to +18.9 and from 209 to 611 Ma, respectively (Table 5; Fig. 11).

5. Discussion

5.1. Timing of magmatism and mineralization

According to previous studies, widespread magmatism occurred in the eastern Tianshan orogenic belt (Mao et al., 2005; Wang et al., 2006; Tang et al., 2007; Zhou et al., 2010; Wang et al., 2015b, c), and the abundant intrusive rocks, including granodiorite, tonalite, quartz porphyry, granite porphyry, biotite granite, monzogranite, syenogranite, A-type granite and alkali-feldspar granite (Liu et al., 2007; Qin et al., 2011; Han et al., 2014; Zhang et al., 2015a, b), are mainly divided into two magmatic stages: Paleozoic and Mesozoic. Magmatic activity during these two episodes showed a close temporal and spatial relationship with Cu (\pm Ni), Mo, Au, Fe and Ag mineral systems, whereas the Late Paleozoic is considered to have been the most important magmatic-metallogenetic episode in eastern Tianshan (Mao et al., 2005; Pirajno et al., 2011; Wang et al., 2015b, c). However, numerous zircon U–Pb dates and Rb–Sr dates on host rocks have revealed some Early Paleozoic magmatic events in the Tianshan orogen (Zhang et al., 2008; Shu et al., 2004). These magmatic rocks mainly include the Mishigou gabbro (468 Ma; Shu et al., 1999), monzogranite (470 ± 3.0 Ma; Gu et al., 1999) and granite (435 Ma; Hopson et al., 1989) in Central Tianshan, and the Sanchakou granodiorite (443 ± 2.9 Ma; Wang et al. 2015f), Xingxingxia granodiorite (424.9 ± 5.8 Ma; Lei et al., 2011) and Weiya granulite (432 ± 1 Ma; Shu et al., 2004) in eastern Tianshan, which represent a significant Early Paleozoic magmatic hydrothermal event. Moreover, the LA-ICP-MS zircon U–Pb dating results in this study indicate that the Yuhai diorite was emplaced at 441.2 ± 2.5 Ma, while the granodiorite formed at

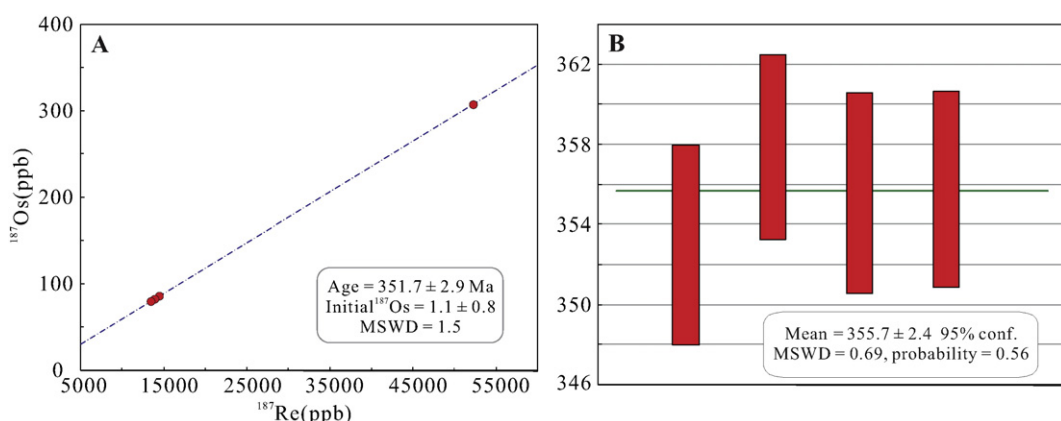


Fig. 7. Re–Os isochron diagram and weighted average model age diagram for four molybdenite samples in the Yuhai porphyry Cu–Mo deposit.

Table 4

Whole-rock geochemical data of the Yuhai diorite and granodiorite in eastern Tianshan (Major elements: wt.%; Trace elements: ppm).

Sample no.	14YH-1	14YH-8	14YH-3	14YH-5	14YH-6	14YH-7	14YH-4	YH-1	YH-2	YH-4	YH-6	YH-7	YH-9
Reference	This study	This study	Zang (2014)										
Rock type	Granodiorite	Granodiorite	Granodiorite	Granodiorite	Granodiorite	Granodiorite	Diorite	Diorite	Diorite	Diorite	Diorite	Diorite	Diorite
SiO ₂	63.17	62.87	63.25	63.33	64.32	64.29	61.30	60.72	58.30	62.27	62.57	61.10	62.86
TiO ₂	0.39	0.39	0.41	0.40	0.36	0.36	0.40	0.54	0.53	0.42	0.42	0.38	0.39
Al ₂ O ₃	17.21	17.39	17.23	17.36	17.17	17.05	16.91	17.36	17.35	16.56	16.18	15.24	16.90
TFe ₂ O ₃	5.22	5.57	5.84	5.65	5.22	5.35	5.49	6.39	7.96	6.94	6.76	7.58	5.34
MnO	0.06	0.06	0.10	0.09	0.08	0.08	0.06	0.13	0.16	0.19	0.18	0.14	0.14
MgO	2.55	1.91	1.93	1.88	1.84	1.94	2.63	2.64	2.70	2.43	2.86	4.80	1.95
CaO	4.18	5.67	5.98	6.00	5.79	5.62	4.48	4.70	5.29	5.02	4.39	4.19	5.03
Na ₂ O	4.18	4.13	3.85	4.05	3.80	3.52	3.99	5.89	3.68	3.53	3.14	3.53	4.44
K ₂ O	1.33	0.41	0.66	0.58	0.42	0.46	0.63	0.43	0.52	0.60	0.74	0.44	1.31
P ₂ O ₅	0.21	0.25	0.21	0.20	0.20	0.20	0.23	0.28	0.26	0.21	0.20	0.18	0.20
LOI	1.49	1.32	0.54	0.44	0.79	1.11	3.37	1.11	3.29	2.10	2.88	2.71	1.50
Total	99.99	99.98	99.99	99.98	99.99	99.98	99.50	100.19	100.04	100.27	100.32	100.29	100.06
Na ₂ O + K ₂ O	5.51	4.54	4.51	4.63	4.22	3.98	4.62	6.32	4.20	4.13	3.88	3.97	5.75
Mg [#]	49	41	40	40	41	42	49	45	40	41	46	56	42
A/CNK	1.08	0.99	0.96	0.95	1.00	1.03	1.10	0.93	1.07	1.06	1.16	1.10	0.94
A/NK	2.07	2.40	2.45	2.38	2.56	2.71	2.33	1.71	2.62	2.56	2.71	2.42	1.94
FeO	2.47	2.92	3.36	2.81	3.18	2.52	1.91	2.94	2.66	3.14	3.4	3.6	2.42
TFe ₂ O ₃ /MgO	2.05	2.92	3.03	3.01	2.84	2.76	2.09	2.42	2.95	2.86	2.36	1.58	2.74
Li	2.06	3.77	3.48	2.54	5.4	6.16	3.98						
Be	0.831	0.964	0.783	0.929	0.638	0.58	0.853						
Sc	10.9	9.52	10.5	9.88	9.9	8.75	13.3						
V	102	84	87	75.5	91.3	74	114	106	120	104	98.4	92.7	71.7
Cr	60.9	97.5	104	71	101	75.4	72.5	37.1	21.3	16.5	82.6	133	9.8
Co	4.07	11.5	13	10.4	8	7.69	20	16.5	25.6	14.8	13.8	34.9	10.1
Ni	4.95	5.44	6.1	4.93	5.45	4.86	5.4						
Cu	87.3	116	343	19.8	204	325	210	62.4	910	240	154	594	14.2
Zn	42.1	37.8	63.8	57.9	41.4	42.2	46.1						
Ga	16.2	18.5	17.8	17.2	17.7	16.3	18.4						
Rb	30.5	5.92	10.1	8.69	6.34	5.83	11.3						
Sr	609	913	786	770	866	781	772	790	816	779	709	607	759
Y	12.7	13.9	14.6	13.5	11.5	10.6	17.4	15.5	10.3	15.2	14.2	14.6	12.8
Zr	71.2	84.2	79.4	76.3	73.4	65.4	78.7	82.6	73.1	61.5	65.6	63.5	70.9
Nb	2.73	7.57	2.18	1.99	2.44	1.87	2.83	3.72	2.78	2.52	2.61	2.33	2.31
Cs	0.24	0.096	0.152	0.155	0.083	0.092	0.198	0.12	0.13	0.15	0.16	0.15	0.3
Ba	457	430	842	637	416	321	336	218	416	498	326	375	754
La	20.1	43.8	18	16.1	11.6	15	14.2	19.8	8.48	16.5	16.3	16	14.9
Ce	35.5	76.3	34.2	31.1	21.3	27.9	27.5	41.7	19.4	35.1	33.6	32.9	32.3
Pr	4.37	8.43	4.4	4.1	2.92	3.51	3.76	5.52	2.52	4.55	4.32	4.16	4.1
Nd	17.8	33.7	18.6	17.8	13.1	14.9	17.3	23.2	10.4	18.6	17.8	17.2	16.7
Sm	3.12	5.35	3.52	3.36	2.57	2.72	3.74	4.79	2.47	3.85	3.6	3.61	3.5
Eu	1.01	1.66	1.24	1.11	1.08	1.05	1.15	1.3	0.99	1.22	1.06	1.13	1.15
Gd	2.75	4.13	2.77	2.53	2.28	2.35	3.14	3.89	2.3	3.42	3.18	3.17	3
Tb	0.498	0.577	0.481	0.481	0.336	0.419	0.554	0.55	0.33	0.5	0.47	0.46	0.43
Dy	2.44	2.8	2.55	2.86	1.91	2.03	3.25	3.06	1.89	2.9	2.74	2.76	2.59
Ho	0.486	0.452	0.49	0.441	0.378	0.371	0.552	0.6	0.39	0.61	0.57	0.57	0.53
Er	1.33	1.33	1.34	1.34	1.23	1.21	1.84	1.72	1.17	1.76	1.7	1.65	1.52
Tm	0.253	0.238	0.235	0.291	0.213	0.181	0.318	0.27	0.2	0.28	0.28	0.28	0.24
Yb	1.6	1.6	1.38	1.53	1.3	1.26	1.93	1.86	1.45	1.98	1.89	1.9	1.7
Lu	0.223	0.25	0.258	0.295	0.258	0.208	0.344	0.28	0.24	0.31	0.3	0.3	0.27
Hf	2.25	2.53	2.57	2.24	2.27	2.13	2.35	2.49	2.3	1.95	2.1	2.02	2.29
Ta	0.238	0.165	0.135	0.118	0.122	0.129	0.196	0.43	0.3	0.26	0.27	0.25	0.27
Pb	7.4	6.26	6	5.18	4.73	4.79	3.87	3.73	11.3	6.85	5.25	5.54	13
Th	1.89	3.61	1.23	1.17	1.56	1.46	1.8	2.25	1.79	1.58	1.6	1.44	1.27
U	1.46	5.12	0.658	0.58	0.886	0.871	1.23	1.04	0.94	0.72	0.69	0.72	0.63
(La/Yb) _N	9.01	19.64	9.36	7.55	6.40	8.54	5.28	7.64	4.19	5.98	6.19	6.04	6.29
Eu/Eu [*]	1.05	1.08	1.21	1.16	1.36	1.27	1.03	0.92	1.27	1.03	0.96	1.02	1.08
Sr/Y	47.95	65.68	53.84	57.04	75.30	73.68	44.37	50.97	79.22	51.25	49.93	41.58	59.30
La/Yb	12.56	27.38	13.04	10.52	8.92	11.90	7.36	10.65	5.85	8.33	8.62	8.42	8.76
Zr + Nb + Ce + Y	122.13	181.97	130.38	122.89	108.64	105.77	126.43	143.52	105.58	114.32	116.01	113.33	118.31
10,000Ga/Al	1.78	2.01	1.95	1.87	1.95	1.81	2.06						

LOI = loss on ignition. A/CNK = molecular Al₂O₃ / (CaO + Na₂O + K₂O); A/NK = molecular Al₂O₃ / (Na₂O + K₂O). Mg[#] = 100 × molecular Mg²⁺ / (Mg²⁺ + Fe²⁺), calculated by assuming TFeO = 0.9 × TFe₂O₃. Eu/Eu^{*} = Eu_N / (Sm_N × Gd_N)^{1/2}, the subscript of N means normalized to chondrite (Sun and McDonough, 1989).

430.4 ± 2.9 Ma to 430.3 ± 2.6 Ma. The geochronology data confirms that they were intruded in the Early Silurian. These data and previous geological data demonstrate that the Early Paleozoic magmatic activity was also developed in the eastern Tianshan orogenic belt (Fig. 1C).

In addition, the internally concordant Re-Os model ages of four molybdenite samples from the Yuhai deposit implies that the Re-Os system had been closed, and the molybdenite Re-Os ages can therefore represent its depositional age. Therefore, the weighted mean model

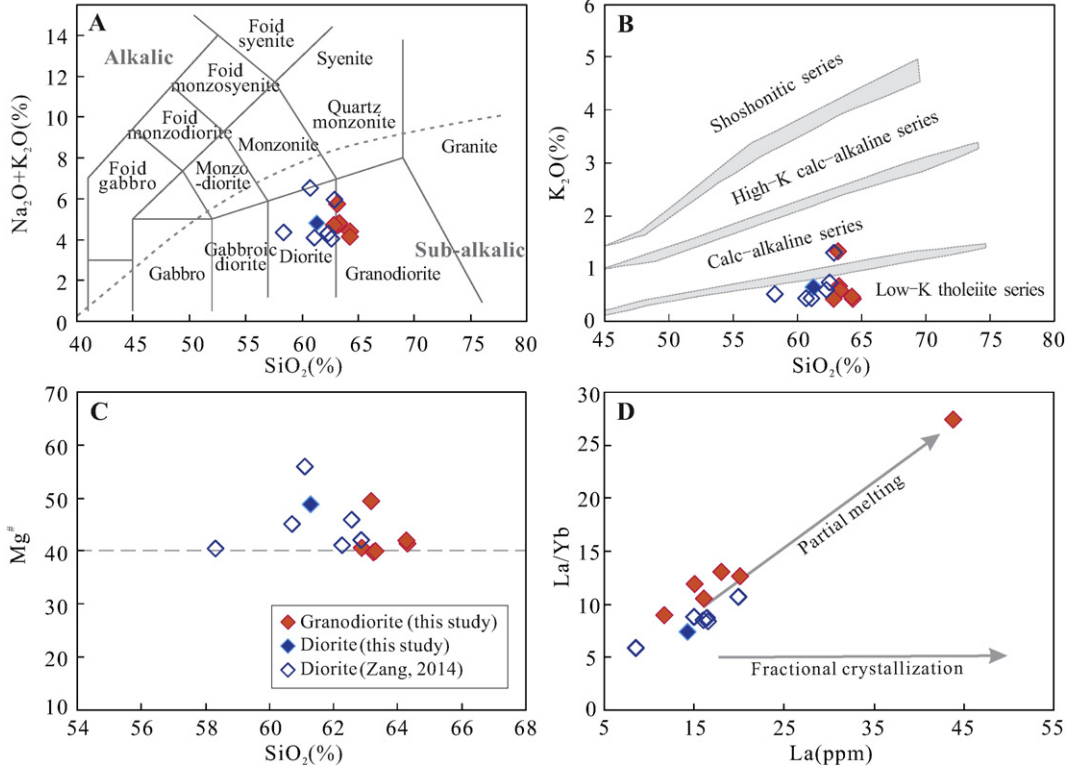


Fig. 8. Classification and diagrams of the Yuhai intrusions. (A) $\text{Na}_2\text{O} + \text{K}_2\text{O}$ vs. SiO_2 diagram (Le Maitre, 2002); (B) K_2O vs. SiO_2 diagram (Rollinson, 1993); (C) $\text{Mg}^\#$ vs. SiO_2 diagram; (D) La/Sm vs. La diagram.

age (355.7 ± 2.4 Ma) of the four analyses precisely dates the hydrothermal deposition of molybdenite at Yuhai. Combined with the new LA-ICP-MS zircon U-Pb ages presented herein (441–430 Ma), the Re-Os isotopic ages (355.7 ± 2.4 Ma) obtained in this study indicate that the Cu mineralization in the Yuhai area occurred later than the intrusive rock emplacement there. Based on the crosscutting relationships, the molybdenite-bearing veinlets associated with phyllitic alteration are present in the diorite and granodiorite. They also indicate that the Re-Os ages of the molybdenite should be later than the intrusion age of the diorite and granodiorite and may be the same as the late ore-forming age at Yuhai. Such a discrepancy has been interpreted to be related to the involvement of multiple hydrothermal events. Zang (2014) indicated that certain Carboniferous intrusions developed in the southern Yuhai area. This is comparable to the situation of the Tuwu-Yandong porphyry Cu deposits located in eastern Tianshan. For example, a range of zircon U-Pb ages from 361.8 ± 7.8 to 332.2 ± 2.3 Ma for plagiogranite porphyry (Rui et al., 2002; Wang et al., 2015b, c), Re-Os isotopic ages of 189–195 Ma for Cu-mineralized plagiogranite porphyry (Gao et al., 2015), K-Ar age of 341.2 ± 4.9 Ma (Qin et al., 2002) and Re-Os isotopic ages of 323–343 Ma for molybdenite (Rui et al., 2002; Zhang et al., 2008) have been obtained in the Tuwu-Yandong deposits. Therefore, multiple hydrothermal events may have been important for the formation of the Yuhai porphyry Cu deposits.

5.2. Petrogenesis and source of the magma

The petrochemical signatures of intrusive rocks record important information on magma sources (Barbarin, 1999; Chen et al., 2007), magmatic processes (Sylvester, 1998; Deng and Wang, 2015; Deng et al., 2015b; Zhu et al., 2011) and tectonic settings (Sillitoe, 1972, 2010; Wu et al., 2007; Wang et al., 2015e; Zhang et al., 2016); therefore, it is important to have a clear understanding of the petrogenetic history of

the Yuhai intrusions. The Yuhai intrusions mainly consist of diorite and granodiorite, with SiO_2 contents ranging from 58.30 to 64.32 wt.%, Al_2O_3 contents ranging from 15.24 to 17.39 wt.% and MgO contents ranging from 1.84 to 4.80 wt.% (Table 4). They have relatively high Sr concentrations (607–913 ppm) and low Y (10.3–17.4 ppm) and HREE concentrations ($\text{Yb} = 1.26$ –1.98 ppm), with geochemical compositions similar to those of modern adakites (Defant et al., 1991). However, compared to adakites, the Yuhai intrusions contain slightly lower SiO_2 and higher MgO contents (Fig. 8C). They also show lower abundances of LREE and LILE (Fig. 10) and variable Y and Yb_N values (Table 4) relative to adakites (Defant et al., 1991) and plot in a transitional adakite to typical arc field in the Sr/Y vs. Y and $(\text{La}/\text{Yb})_N$ vs. Yb_N diagrams (Fig. 12A, B; Defant and Drummond, 1990).

The Yuhai dioritic and granodioritic intrusions have similar geochemical characteristics that indicate a relatively uniform and integrated magmatic origin beneath eastern Tianshan. In detail, they are characterized by a strong LREE enrichment, moderate HREE depletion and slightly positive Eu anomalies that reflect clear subduction signatures. They also have less variable La contents but variation in the La/Yb ratios, which suggest that the partial melting process was dominant in their petrogenesis (Fig. 8D). In addition, the Yuhai intrusions show pronounced depletions of Nb, Ta and Ti and enrichments of K, Rb and Pb (Fig. 10B), similar to those of most modern subduction-related plutonic rocks (Wood et al., 1979; Briquet et al., 1984; Shen et al., 2014) formed by the partial melting of subducted oceanic slabs.

Experimental studies have shown that $\text{Mg}^\#$ is a useful criterion for distinguishing melts purely derived from the crust from those involved in the mantle. Melts from the basaltic lower crust are characterized by a low $\text{Mg}^\#$ less than 40 regardless of melting degree, whereas those with $\text{Mg}^\#$ greater than 40 can only be obtained when a mantle component is involved (Rapp and Watson, 1995; Rapp et al., 1999; Guan et al., 2011; Zhu et al., 2009, 2013). All of the Yuhai diorite and granodiorite rocks

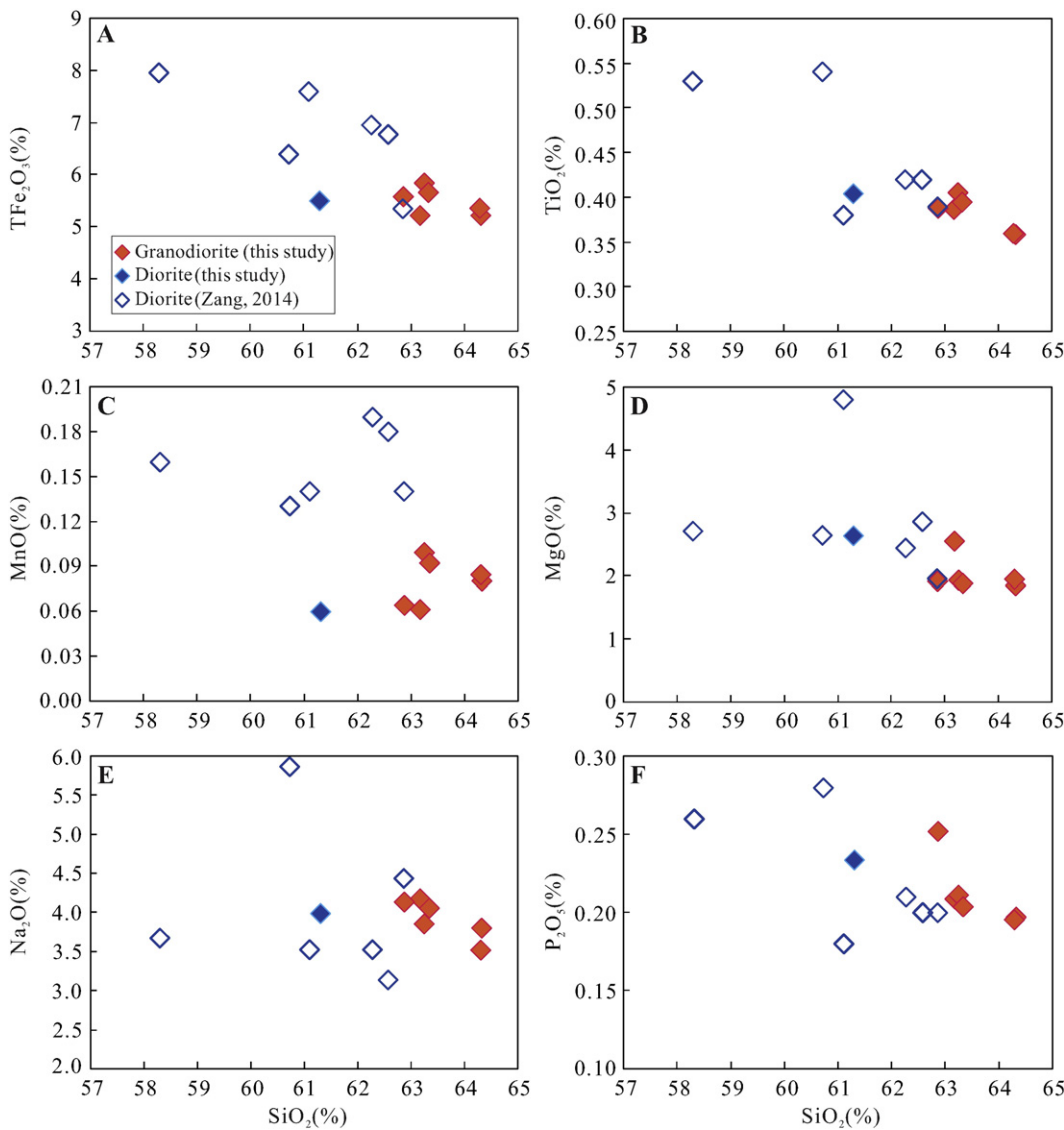


Fig. 9. Harker diagram of intrusions in the Yuhai porphyry Cu–Mo deposit.

show features of high MgO contents (1.84–4.80 wt.%) and Mg[#] values (40–56) (Fig. 8C), which indicate the involvement of mantle components.

These results are supported by the zircon Hf isotopic data (Table 5). The Hf isotopic compositions of the intrusions from the Yuhai area are characterized by positive $\epsilon_{\text{Hf}}(t)$ values, which range from +8.7 to +18.6 of magmatic zircons from a diorite sample (14YH-1) and from +12.6 to +19.6 of zircons from granodiorite samples (14YH-01 and 14YH-02) (Table 5; Fig. 11A). They also show young Hf model ages (T_{DM}^{c}), which are between 234 and 872 Ma (diorite) and between 209 and 612 Ma (granodiorite) (Table 5; Fig. 11B). In the $\epsilon_{\text{Hf}}(t)$ vs. U–Pb age diagram (Fig. 11C), zircons from these samples show a spread of $\epsilon_{\text{Hf}}(t)$ values near the depleted mantle evolution line, which indicates that they were most likely derived from a depleted mantle source. Given the normal island arc affinities and inhomogeneous $\epsilon_{\text{Hf}}(t)$ values (greater than 6.3 ϵ units) recorded in the Yuhai diorite and granodiorite rocks, it is suggested that the melt of those intrusions could be a product of the partial melting of mantle components that were previously metasomatized by slab melts.

Considering the entire dataset, it is proposed that the Yuhai intrusions share similar petrochemical signatures to those formed in an

island arc, namely the Dananhu–Tousuquan arc. The primary magmas for the diorite (~442 Ma) and granodiorite (~430 Ma) intrusions were most likely derived from the partial melting of the subduction-modified mantle components.

5.3. Implications for the geodynamic setting and Cu–Mo mineralization

The intrusive rocks analyzed in this study and in previous research were found to have transitional tholeiitic to calc-alkaline affinities, enriched in LREEs and LILEs (e.g., K, Ba, Pb and Sr) and depleted in HFSEs (e.g., Th, Nb, Ta, and Ti), indicating a magma that formed in a relatively immature island arc setting (Miyashiro, 1974; Liégeois et al., 1998). The granodioritic samples plot within the volcanic arc field in the Rb vs. (Ta + Yb) tectonic discrimination diagram (Fig. 13A; Pearce et al., 1984) and all of the intrusive samples fall between the EMORB and OIB areas in the Th/Yb vs. Nb/Yb diagram (Fig. 13B; Pearce and Peate, 1995; Sayit and Goncuoglu, 2009), which are characteristics of island arc igneous rocks emplaced during the Silurian subduction of an oceanic slab. Their isotopic compositions ($\epsilon_{\text{Hf}}(t) = +8.7$ to +19.6) match that of a depleted mantle source. Thus, we suggest that the Yuhai intrusions were formed in an island arc setting.

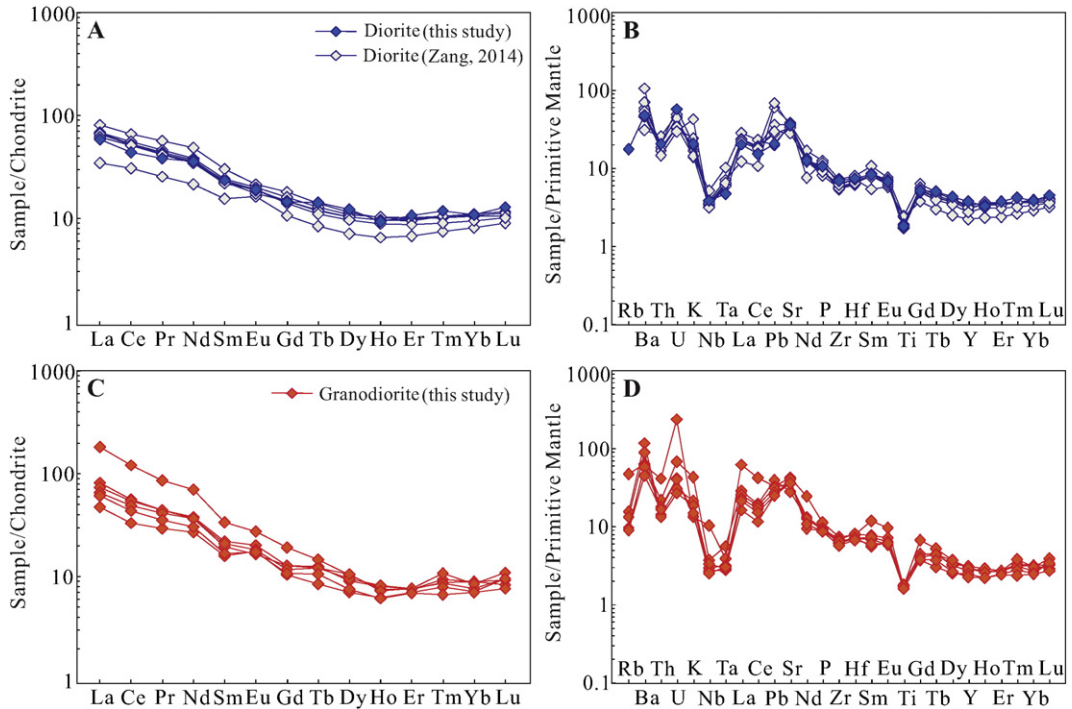


Fig. 10. Chondrite-normalized REE (A, C) and primitive mantle-normalized trace element abundance spider diagram (B, D) for the Yuhai intrusions. Normalized data are from Boynton (1984) and Sun and McDonough (1989).

Most porphyry Cu deposits reported throughout the world occurred in magmatic arcs above subduction zones (Cooke et al., 2005; Seedorff et al., 2005; Sillitoe, 2010) and are associated with calc-alkaline magmas (Richards, 2003; Hou et al., 2013). Those deposits include the El Teniente, Río Blanco–Los Bronces and Los Pelambres porphyry Cu deposits in central Chile (Reich et al., 2003; Jiang et al., 2010), the Chuquicamata porphyry Cu deposit in northern Chile (Barra et al., 2013), the Arynnuur porphyry Mo deposit in East Mongolia (Liu et al., 2010) and the Tuwu–Yandong–Linglong–Chihu porphyry Cu deposits in North Xinjiang (Zhang et al., 2008; Wang et al., 2014; Xiao et al., 2015b). Therefore, magmatic arcs above subduction zones have been shown to be favorable tectonic settings for the generation of porphyry Cu deposits (Defant et al., 2002; Reich et al., 2003; Sun et al., 2010; Yang et al., 2012, 2014).

As reported in previous studies, widespread Paleozoic–Mesozoic granitoids and volcanic rocks were emplaced in eastern Tianshan orogenic belt (Fig. 1C; Wang et al., 2006; Chen et al., 2012b, 2014) during a complex tectonic–magmatic evolution that included subduction and accretion followed by the collision between the Siberian and Tarim Cratons (Han et al., 2006; Xiao et al., 2010, 2013; Santosh et al., 2011). Recently, a large number of Paleozoic (443–322 Ma) rocks with arc affinity have been reported in the Dananhu–Tousuquan arc belt, including Sanchakou granodiorites (443 ± 2.9 Ma; Wang et al., 2015f), Yuhai diorites and granodiorites (441.6 ± 2.5 Ma, and 430.4 ± 2.9 Ma and 430.3 ± 2.6 Ma, respectively; this study), Dananhu granodiorites and monzogranites (357.3 ± 6.2 and 383 ± 9 Ma, respectively; Song et al., 2002), Yandong diorite porphyries and tonalites (340 ± 3 and 335 ± 3.7 Ma, respectively; Shen et al., 2014; Wang et al., 2015b), Tuwu tonalites (332.3 ± 5.9 Ma; Wang et al., 2015c) and Chihu tonalites (320.2 ± 2.4 Ma; Zhang et al., 2015b), which are interpreted to be related to subduction tectonic settings. This indicates that the subduction of the ancient Tianshan Ocean most likely began in the Silurian (Xiao et al., 2013; Wang et al., 2015f; Zhao et al., 2015). On the basis of previous studies, the geodynamics of the eastern Tianshan orogenic belt can be summarized in two stages: the double-sided subduction of the ancient Tianshan oceanic plate, which was probably initiated during the Silurian to Carboniferous and led to the formation of the Dananhu–Tousuquan

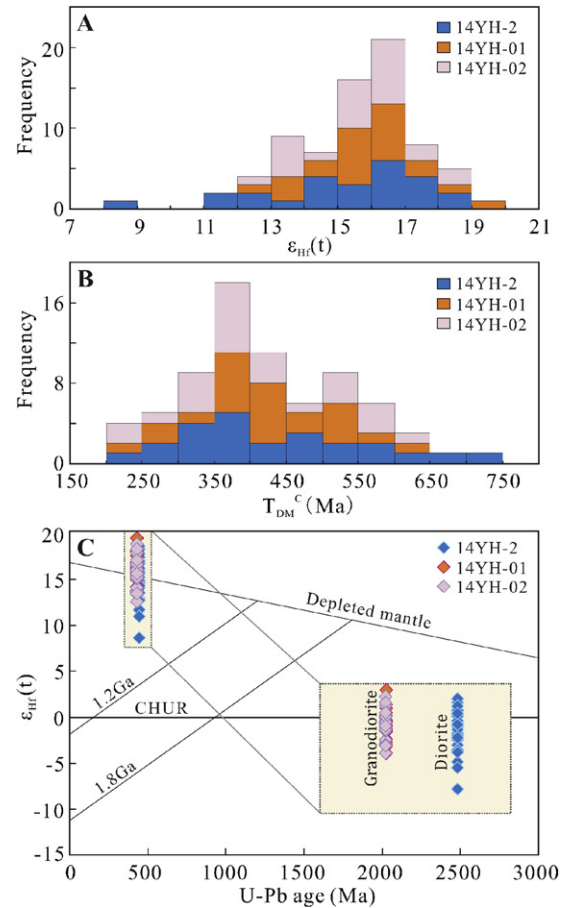


Fig. 11. (A) Histogram of zircon $\epsilon_{\text{Hf}}(t)$ values; (B) Histogram of zircon Hf-isotope crust model age (T_{DM}^c) (Ma); (C) Correlation diagrams of zircon Hf isotopes versus U–Pb ages of the Yuhai intrusions. The concentration of Hf in N-type MORB from Sun and McDonough (1989) is used to represent the composition of melt derived from depleted mantle.

Table 5

Zircon Hf isotopic data for the Yuhai diorite and granodiorite in eastern Tianshan.

Spot	Age/Ma	$^{176}\text{Yb}/^{177}\text{Hf}$	$^{176}\text{Lu}/^{177}\text{Hf}$	$^{176}\text{Hf}/^{177}\text{Hf}$	$\pm 2\sigma$	$^{176}\text{Hf}/^{177}\text{Hf(t)}$	$^{176}\text{Hf}/^{177}\text{Hf CHUR(t)}$	$\varepsilon_{\text{Hf}}(0)$	$\varepsilon_{\text{Hf}}(\text{t})$	$\pm 2\sigma$	T_{DM}/Ma	$T_{\text{DM}}^{\text{C}}/\text{Ma}$	$f_{\text{Lu/Hf}}$
<i>14YH-2, diorite, 441.6 ± 2.5 Ma, $\varepsilon_{\text{Hf}}(\text{t}) = +8.7 \text{ to } +18.6$</i>													
14YH-2 01	441	0.034348	0.001412	0.282928	0.000037	0.282916	0.282498	5.5	14.8	1.3	464	478	-0.96
14YH-2 02	441	0.024006	0.001184	0.282920	0.000037	0.282910	0.282498	5.2	14.6	1.3	474	493	-0.96
14YH-2 03	442	0.035177	0.001696	0.282987	0.000039	0.282973	0.282497	7.6	16.9	1.4	382	348	-0.95
14YH-2 04	445	0.040487	0.001926	0.282984	0.000042	0.282968	0.282495	7.5	16.7	1.5	389	357	-0.94
14YH-2 05	442	0.026827	0.001327	0.282980	0.000044	0.282969	0.282497	7.4	16.7	1.5	389	358	-0.96
14YH-2 06	431	0.028669	0.001233	0.282912	0.000031	0.282903	0.282504	5.0	14.1	1.1	484	516	-0.96
14YH-2 07	441	0.027321	0.001302	0.282981	0.000036	0.282970	0.282498	7.4	16.7	1.3	388	356	-0.96
14YH-2 08	442	0.042901	0.002036	0.283031	0.000035	0.283014	0.282497	9.1	18.3	1.2	322	256	-0.94
14YH-2 09	442	0.031226	0.001514	0.282965	0.000038	0.282953	0.282497	6.8	16.1	1.3	412	394	-0.95
14YH-2 10	442	0.033805	0.001651	0.283003	0.000038	0.282989	0.282497	8.2	17.4	1.3	359	311	-0.95
14YH-2 11	440	0.036792	0.001764	0.282971	0.000042	0.282957	0.282498	7.1	16.2	1.5	406	386	-0.95
14YH-2 12	440	0.031395	0.001544	0.282893	0.000039	0.282881	0.282498	4.3	13.5	1.4	516	559	-0.95
14YH-2 13	442	0.028528	0.001392	0.283035	0.000040	0.283024	0.282497	9.3	18.6	1.4	310	234	-0.96
14YH-2 14	442	0.038289	0.001847	0.282878	0.000048	0.282862	0.282497	3.7	12.9	1.7	543	600	-0.94
14YH-2 15	440	0.028915	0.001381	0.282950	0.000043	0.282939	0.282498	6.3	15.6	1.5	432	427	-0.96
14YH-2 16	442	0.037301	0.001824	0.282942	0.000041	0.282927	0.282497	6.0	15.2	1.4	449	452	-0.95
14YH-2 17	442	0.040818	0.001925	0.282959	0.000041	0.282944	0.282497	6.6	15.8	1.5	425	415	-0.94
14YH-2 18	442	0.032089	0.001523	0.282839	0.000038	0.282826	0.282497	2.4	11.7	1.4	594	681	-0.95
14YH-2 19	442	0.042589	0.002050	0.282874	0.000041	0.282857	0.282497	3.6	12.7	1.4	551	612	-0.94
14YH-2 20	441	0.028189	0.001399	0.282754	0.000046	0.282742	0.282498	-0.7	8.7	1.6	714	872	-0.96
14YH-2 21	440	0.039955	0.001892	0.282918	0.000042	0.282903	0.282498	5.2	14.3	1.5	484	509	-0.94
14YH-2 22	441	0.025446	0.001263	0.282999	0.000037	0.282989	0.282498	8.0	17.4	1.3	361	313	-0.96
14YH-2 23	443	0.028898	0.001389	0.283011	0.000039	0.283000	0.282496	8.5	17.8	1.4	344	287	-0.96
14YH-2 24	443	0.034388	0.001660	0.282992	0.000043	0.282978	0.282496	7.8	17.1	1.5	375	336	-0.95
14YH-2 25	443	0.036746	0.001751	0.282822	0.000037	0.282807	0.282496	1.8	11.0	1.3	622	724	-0.95
<i>14YH-01, granodiorite, 430.4 ± 2.9 Ma, $\varepsilon_{\text{Hf}}(\text{t}) = +12.6 \text{ to } +19.6$</i>													
14YH-01 01	492	0.031554	0.001703	0.282964	0.000034	0.282949	0.282466	6.8	17.1	1.2	415	372	-0.95
14YH-01 02	430	0.019915	0.001078	0.282972	0.000031	0.282963	0.282504	7.1	16.2	1.1	398	378	-0.97
14YH-01 03	431	0.029059	0.001549	0.283013	0.000029	0.283001	0.282504	8.5	17.6	1.0	343	293	-0.95
14YH-01 04	432	0.026152	0.001371	0.282968	0.000030	0.282956	0.282503	6.9	16.0	1.1	407	392	-0.96
14YH-01 05	432	0.016458	0.000884	0.282910	0.000031	0.282903	0.282503	4.9	14.2	1.1	483	514	-0.97
14YH-01 06	432	0.021261	0.001180	0.282869	0.000030	0.282860	0.282503	3.4	12.6	1.0	545	612	-0.96
14YH-01 07	431	0.022341	0.001223	0.282915	0.000028	0.282905	0.282504	5.1	14.2	1.0	480	509	-0.96
14YH-01 08	431	0.026371	0.001372	0.282976	0.000030	0.282965	0.282504	7.2	16.3	1.1	394	373	-0.96
14YH-01 09	430	0.031134	0.001641	0.282971	0.000032	0.282957	0.282504	7.0	16.0	1.1	406	392	-0.95
14YH-01 10	427	0.027164	0.001481	0.283028	0.000034	0.283016	0.282506	9.1	18.0	1.2	321	260	-0.96
14YH-01 11	430	0.020346	0.001138	0.282892	0.000030	0.282883	0.282504	4.2	13.4	1.1	512	561	-0.97
14YH-01 12	391	0.024424	0.001330	0.282929	0.000027	0.282920	0.282529	5.6	13.8	1.0	461	502	-0.96
14YH-01 13	456	0.027396	0.001489	0.282957	0.000032	0.282945	0.282488	6.6	16.2	1.1	423	404	-0.96
14YH-01 14	444	0.033451	0.001792	0.282955	0.000030	0.282940	0.282496	6.5	15.7	1.1	430	422	-0.95
14YH-01 15	430	0.025480	0.001365	0.282942	0.000030	0.282931	0.282504	6.0	15.1	1.1	443	451	-0.96
14YH-01 16	430	0.019632	0.001073	0.282898	0.000027	0.282889	0.282504	4.5	13.6	1.0	503	546	-0.97
14YH-01 17	427	0.033102	0.001758	0.282951	0.000028	0.282937	0.282506	6.3	15.2	1.0	436	441	-0.95
14YH-01 18	428	0.031756	0.001683	0.282943	0.000028	0.282930	0.282506	6.1	15.0	1.0	446	456	-0.95
14YH-01 19	431	0.030915	0.001590	0.282950	0.000029	0.282937	0.282504	6.3	15.3	1.0	435	438	-0.95
14YH-01 20	431	0.034569	0.001745	0.282993	0.000028	0.282979	0.282504	7.8	16.8	1.0	374	342	-0.95
14YH-01 21	431	0.020570	0.000966	0.282952	0.000028	0.282944	0.282504	6.4	15.6	1.0	425	422	-0.97
14YH-01 22	496	0.022637	0.001180	0.283028	0.000031	0.283017	0.282463	9.1	19.6	1.1	318	213	-0.96
14YH-01 23	455	0.036005	0.001765	0.282943	0.000028	0.282928	0.282489	6.1	15.6	1.0	446	442	-0.95
14YH-01 24	430	0.017464	0.000842	0.282965	0.000027	0.282958	0.282504	6.8	16.1	1.0	405	390	-0.97
<i>14YH-02, granodiorite, 430.3 ± 2.6 Ma, $\varepsilon_{\text{Hf}}(\text{t}) = +12.6 \text{ to } +18.9$</i>													
14YH-02 01	432	0.015637	0.000818	0.282897	0.000027	0.282890	0.282503	4.4	13.7	1.0	501	543	-0.98
14YH-02 02	431	0.031375	0.001444	0.283021	0.000027	0.283009	0.282504	8.8	17.9	0.9	331	273	-0.96
14YH-02 03	431	0.035621	0.001850	0.282987	0.000031	0.282972	0.282504	7.6	16.6	1.1	384	357	-0.94
14YH-02 04	429	0.028388	0.001501	0.282967	0.000028	0.282955	0.282505	6.9	15.9	1.0	410	398	-0.95
14YH-02 05	432	0.034201	0.001744	0.282905	0.000027	0.282891	0.282503	4.7	13.7	0.9	501	540	-0.95
14YH-02 06	431	0.042417	0.002131	0.282972	0.000029	0.282955	0.282504	7.1	16.0	1.0	409	396	-0.94
14YH-02 07	432	0.025975	0.001328	0.282969	0.000027	0.282958	0.282503	7.0	16.1	1.0	404	388	-0.96
14YH-02 08	423	0.018853	0.000974	0.282915	0.000025	0.282907	0.282509	5.1	14.1	0.9	477	510	-0.97
14YH-02 09	444	0.041787	0.002061	0.282892	0.000030	0.282875	0.282496	4.2	13.4	1.1	525	570	-0.94
14YH-02 10	430	0.023735	0.001234	0.282871	0.000028	0.282861	0.282504	3.5	12.6	1.0	544	611	-0.96
14YH-02 11	430	0.024359	0.001297	0.282982	0.000028	0.282972	0.282504	7.4	16.6	1.0	385	358	-0.96
14YH-02 12	430	0.024987	0.001329	0.282897	0.000026	0.282886	0.282504	4.4	13.5	0.9	508	554	-0.96
14YH-02 13	430	0.033906	0.001793	0.283052	0.000027	0.283038	0.282504	9.9	18.9	1.0	289	209	-0.95
14YH-02 14	430	0.021926	0.001198	0.282941	0.000030	0.282931	0.282504	6.0	15.1	1.1	443	451	-0.96
14YH-02 15	430	0.058152	0.002931	0.282963	0.000030	0.282939	0.282504	6.7					

Table 5 (continued)

Spot	Age/Ma	$^{176}\text{Yb}/^{177}\text{Hf}$	$^{176}\text{Lu}/^{177}\text{Hf}$	$^{176}\text{Hf}/^{177}\text{Hf}$	$\pm 2\sigma$	$^{176}\text{Hf}/^{177}\text{Hf(t)}$	$^{176}\text{Hf}/^{177}\text{Hf CHUR(t)}$	$\varepsilon_{\text{Hf}}(0)$	$\varepsilon_{\text{Hf}}(\text{t})$	$\pm 2\sigma$	T_{DM}/Ma	$T_{\text{DM}}^{\text{C}}/\text{Ma}$	$f_{\text{Lu/Hf}}$
14YH-02 22	431	0.016909	0.000880	0.282953	0.000028	0.282946	0.282504	6.4	15.6	1.0	423	417	-0.97
14YH-02 23	431	0.026938	0.001419	0.282896	0.000032	0.282884	0.282504	4.4	13.5	1.1	511	557	-0.96
14YH-02 24	429	0.035169	0.001843	0.283036	0.000031	0.283021	0.282505	9.3	18.3	1.1	313	247	-0.94
14YH-02 25	433	0.020494	0.000984	0.282993	0.000029	0.282985	0.282503	7.8	17.1	1.0	366	327	-0.97

$$\varepsilon_{\text{Hf}}(\text{t}) = 10,000 \times \left[\left(\left(\frac{^{176}\text{Hf}}{^{177}\text{Hf}} \right)_S - \left(\frac{^{176}\text{Lu}}{^{177}\text{Hf}} \right)_S \times (e^{\lambda t} - 1) \right) / \left[\left(\frac{^{176}\text{Hf}}{^{177}\text{Hf}} \right)_{\text{CHUR,0}} - \left(\frac{^{176}\text{Lu}}{^{177}\text{Hf}} \right)_{\text{CHUR}} \times (e^{\lambda t} - 1) \right] - 1 \right],$$

$$T_{\text{DM}} = 1/\lambda \times \ln(1 + \left[\left(\frac{^{176}\text{Hf}}{^{177}\text{Hf}} \right)_S - \left(\frac{^{176}\text{Hf}}{^{177}\text{Hf}} \right)_{\text{DM}} \right] / \left[\left(\frac{^{176}\text{Hf}}{^{177}\text{Hf}} \right)_S - \left(\frac{^{176}\text{Hf}}{^{177}\text{Hf}} \right)_{\text{DM}} \right]),$$

$$T_{\text{DM}}^{\text{C}} = T_{\text{DM}} - (T_{\text{DM}} - t) \times \left[(f_{cc} - f_s) / (f_{cc} - f_{DM}) \right],$$

$$f_{\text{Lu/Hf}} = \left(\frac{^{176}\text{Lu}}{^{177}\text{Hf}} \right)_S / \left(\frac{^{176}\text{Lu}}{^{177}\text{Hf}} \right)_{\text{CHUR}} - 1,$$

where, $\lambda = 1.867 \times 10^{-11} \text{ year}^{-1}$ (Soderlund et al., 2004); $(^{176}\text{Lu}/^{177}\text{Hf})_S$ and $(^{176}\text{Hf}/^{177}\text{Hf})_S$ are the measured values of the samples; $(^{176}\text{Lu}/^{177}\text{Hf})_{\text{CHUR}} = 0.0332$ and $(^{176}\text{Hf}/^{177}\text{Hf})_{\text{CHUR,0}} = 0.282772$ (Blichert-Toft and Albarède, 1997); $(^{176}\text{Lu}/^{177}\text{Hf})_{\text{DM}} = 0.0384$ and $(^{176}\text{Hf}/^{177}\text{Hf})_{\text{DM}} = 0.28325$ (Griffin et al., 2002); $(^{176}\text{Lu}/^{177}\text{Hf})_{\text{mean crust}} = 0.015$; $f_{cc} = [(^{176}\text{Lu}/^{177}\text{Hf})_{\text{mean crust}} / (^{176}\text{Lu}/^{177}\text{Hf})_{\text{CHUR}}] - 1$; $f_s = f_{\text{Lu/Hf}}$; $f_{DM} = [(^{176}\text{Lu}/^{177}\text{Hf})_{\text{DM}} / (^{176}\text{Lu}/^{177}\text{Hf})_{\text{CHUR}}] - 1$; and t = crystallization time of zircon.

arc belt to the north and the Aqishan–Yamansu arc belt to the south, as evidenced by the positive bulk $\varepsilon_{\text{Nd}}(\text{t})$ and zircon $\varepsilon_{\text{Hf}}(\text{t})$ values of the Silurian–Carboniferous granitoids and volcanic rocks in eastern Tianshan (Tang et al., 2010; Lei et al., 2011; Zhao et al., 2015); and a post-collisional stage since the Early Permian, as supported by the presence of the youngest ophiolite of ~310 Ma along with widespread bimodal volcanic rocks of ~290 Ma (Qin et al., 2011; Su et al., 2012; Zhang et al., 2015b). Numerous Cu (\pm Ni), Mo, Au, Fe, and Ag metal deposits and associated magmatic rocks were formed in the periods of subduction and post-collisional tectonism.

Previous studies have shown that throughout the stage of the ancient Tianshan ocean subduction, a double subduction of the ancient Tianshan oceanic plate could have occurred during the Silurian to Carboniferous (Han et al., 2006; Xiao et al., 2010, 2013). The Re concentrations of four molybdenite samples from the Yuhai deposit range from 2.1×10^{-5} to 8.3×10^{-5} , with an average of 3.7×10^{-5} (Table 3), which suggests a mixing origin of the mantle and crust (Mao et al., 1999). Zang (2014) argued that the ^{34}S values of sulfide minerals in the Yuhai deposit exhibit a narrow range (-3 to +0.3‰), which indicates a magmatic source of the sulfur (-3 to +3‰; Chaussidon and Lorand, 1990). Therefore, combined with the regional geological history and our new isotopic age data, we posit that the ancient Tianshan oceanic plate subducted northward beneath the Dananhu–Tousuquan island arc belt and southward beneath the Aqishan–Yamansu island arc belt. Under that subduction-related tectonic setting, the metasomatized mantle magma was emplaced into the shallow crust and induced the formation of the Yuhai intrusions and Cu–Mo deposit, and during that period, the hydrothermal fluids of enriched sulfides possibly played a crucial role in Cu–Mo mineralization.

6. Conclusions

(1) LA-ICP-MS zircon U–Pb dating indicates that magmatic events occurred at ca. 441–430 Ma in the Yuhai area, and the associated

porphyry Cu–Mo deposit formed later than the emplacement of the diorite and granodiorite.

- (2) The geochemical and Hf isotopic data for the diorites and granodiorites in the Yuhai porphyry Cu–Mo deposit indicate that the host rocks were probably derived from the partial melting of the subduction-modified mantle components.
- (3) Based on the regional geological history, new geochronological and geochemical data, we suggest that the Yuhai intrusions and the associated porphyry Cu–Mo mineralization in eastern Tianshan were generated in an arc setting and that they were likely the result of the northward subduction of the ancient Tianshan ocean plate beneath the Dananhu–Tousuquan arc belt during the Silurian to Carboniferous.

Acknowledgements

This research was financially supported by the National Natural Science Foundation of China (41572066 and 41030423), the Fundamental Research Funds for the Central Universities (2652015019 and 2652015032), the Open Research Funds for the State Key Laboratory of Geological Processes and Mineral Resources (GPMR201512) and the Geological Survey Project of China (1212011085471 and 1212011220923). We are very grateful to Editor-in-Chief Franco Pirajno and two reviewers for their constructive comments and assistance in improving the manuscript. We thank Jing Feng of the Xinjiang Bureau of Geology and Mineral Exploration and Jinzhu San and Shoubo Chen of the No. 704 Geological Team of the Xinjiang Nonferrous Geoexploration Bureau for their great support and assistance in our fieldwork. We also appreciate the kind help of Li Su from the China University of Geosciences (Beijing) on the LA-ICP-MS zircon U–Pb dating and Chao Li from the Chinese Academy of Geological Sciences on the Re–Os isotope dating. We thank Chinese

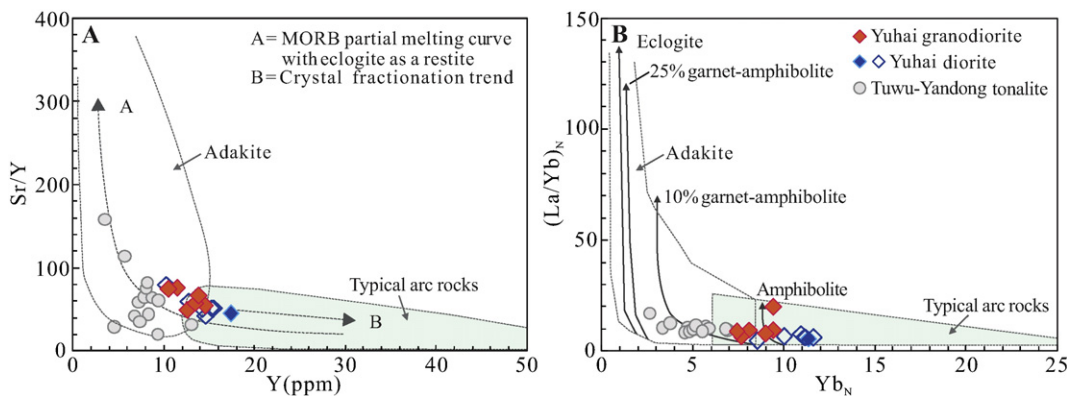


Fig. 12. Plots of Sr/Y vs. Y diagram (A), and $(\text{La}/\text{Yb})_{\text{N}}$ vs. Yb_{N} diagram (B) for the Yuhai intrusions. N means normalized to chondrite (Sun and McDonough, 1989). Modified from Defant and Drummond (1990). Data for the Tuwu-Yandong tonalite are from Wang et al. (2015b,c), and Shen et al. (2012).

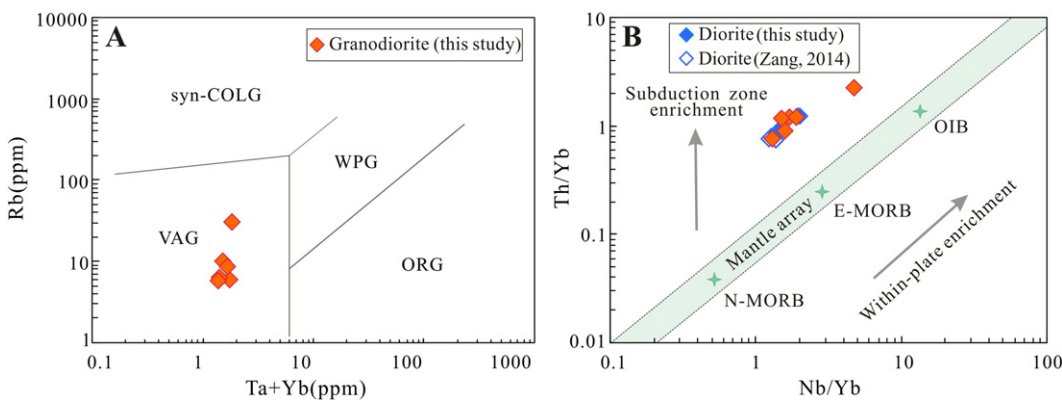


Fig. 13. Tectonic discrimination diagrams for the Yuhai intrusions. (A) Rb vs. Ta + Yb diagram (Pearce et al., 1984); (B) Th/Yb vs. Nb/Yb diagram (Pearce and Peate, 1995; Sayit and Goncuoglu, 2009). WPG, within-plate granitoid; VAG, volcanic arc granitoid; Syn-COLG, syn-collision granitoid; Post-COLG, post-collision granitoid; ORG, ocean ridge granitoid.

Academician Yusheng Zhai of the China University of Geosciences (Beijing) for a helpful scientific review of an earlier version of the manuscript.

References

- Barbarin, B., 1999. A review of the relationships between granitoid types, their origins and their geodynamic environments. *Lithos* 46, 605–626.
- Barra, F., Alcota, H., Rivera, S., Valencia, V., Munizaga, F., Maksaei, V., 2013. Timing and formation of porphyry Cu–Mo mineralization in the Chuquicamata district, northern Chile: new constraints from the Toki cluster. *Mineral. Deposita* 48, 629–651.
- Bgmrxxar (Bureau of Geology and Mineral Resources of Xinjiang Uygur Autonomous Region), 1993n. *Regional Geology of Xinjiang Uygur Autonomous Region*. Geological Publishing House, Beijing 841 pp. (in Chinese with English abstract).
- Blichert-Toft, J., Albarède, F., 1997. The Lu–Hf geochemistry of chondrites and the evolution of the mantle–crust system. *Earth Planet. Sci. Lett.* 148, 243–258.
- Boynton, W.V., 1984. Geochemistry of the rare earth elements, meteorite studies. In: Henderson, P. (Ed.), *Rare Earth Element Geochemistry*. Elsevier, Amsterdam, pp. 63–114.
- Brihuega, L., Bougault, H., Joron, J.L., 1984. Quantification of Nb, Ta, Ti and V anomalies in magmas associated with subduction zones—petrogenetic implications. *Earth Planet. Sci. Lett.* 68, 297–308.
- Cawood, P.A., Kröner, A., Collins, W.J., Kusky, T.M., Mooney, W.D., Windley, B.F., 2009. Earth accretionary orogens through Earth history. In: Cawood, P.A., Kröner, A. (Eds.), *Earth Accretionary Systems in Space and Time: Geological Society of London. Special Publications* 318, pp. 1–36.
- Charvet, J., Shu, L.S., Charvet, S.L., 2007. Paleozoic structural and geodynamic evolution of eastern Tianshan (NW China): welding of the Tarim and Junggar plates. *Episodes* 30, 162–186.
- Chaussidon, M., Lorand, J.P., 1990. Sulphur isotope composition of orogenic spinel lherzolite massifs from Ariège (N.E. Pyrenees, France): an ion microprobe study. *Geochim. Cosmochim. Acta* 54, 2835–2846.
- Chen, H.Y., Yang, J.T., Baker, M., 2012a. Mineralization and fluid evolution of the Jiyuan polymetallic Cu–Ag–Pb–Zn–Au deposit, Eastern Tianshan, NW China. *Int. Geol. Rev.* 54, 816–832.
- Chen, Y.J., Chen, H.Y., Zaw, K., Pirajno, F., Zhang, Z.J., 2007. Geodynamic settings and tectonic model of skarn gold deposits in China: an overview. *Ore Geol. Rev.* 31, 139–169.
- Chen, Y.J., Pirajno, F., Wu, G., Qi, J.P., Xiong, X.L., 2012b. Epithermal deposits in North Xinjiang, NW China. *Int. J. Earth Sci.* 101, 889–917.
- Chen, Y.J., Santosh, M., Somerville, I., Chen, H.Y., 2014. Indosinian tectonics and mineral systems in China: an introduction. *Geol. J.* 49, 331–337.
- Cooke, D.R., Hollings, P., Walsh, J.L., 2005. Giant porphyry deposits: characteristics, distribution, and tectonic controls. *Economic Geology* 100th Anniversary, pp. 801–818.
- Defant, M.J., Drummond, M.S., 1990. Derivation of some modern arc magmas by melting of young subducted lithosphere. *Nature* 347, 662–665.
- Defant, M.J., Richerson, P.M., Deboer, J.Z., Stewart, R.H., Maury, R.C., Bellon, H., Drummond, M.S., Feigenson, M.D., Jackson, T.E., 1991. Dacite genesis via both slab melting and differentiation—petrogenesis of La-Yeguada Volcanic Complex, Panama. *J. Petrol.* 32, 1101–1142.
- Defant, M.J., Xu, J.F., Kepezhinskis, P., Wang, Q., Zhang, Q., Xiao, L., 2002. Adakites: some variations on a theme. *Acta Petrol. Sinica* 18, 129–142.
- Deng, J., Wang, Q.F., Li, G.J., Santosh, M., 2014. Cenozoic tectono-magmatic and metallogenic processes in the Sanjiang region, southwestern China. *Earth-Sci. Rev.* 138, 268–299.
- Deng, J., Wang, Q.F., 2015. Gold mineralization in China: metallogenic provinces, deposit types and tectonic framework. *Gondwana Res.* <http://dx.doi.org/10.1016/j.gr.2015.10.003>.
- Deng, J., Wang, C.M., Bagas, L., Carranza, E.J.M., Lu, Y.J., 2015a. Cretaceous–Cenozoic tectonic history of the Jiaojia Fault and gold mineralization in the Jiaodong Peninsula, China: constraints from zircon U–Pb, illite K–Ar, and apatite fission track thermochronometry. *Mineral. Deposita* 50, 987–1006.
- Deng, J., Wang, Q.F., Li, G.J., Zhao, Y., 2015b. Structural control and genesis of the Oligocene Zhenyuan orogenic gold deposit, SW China. *Ore Geol. Rev.* 65, 42–54.
- Du, A.D., Wu, S.Q., Sun, D.Z., Wang, S.X., Qu, W.J., Richard, M.H.S., John, M., Dmitry, M., 2004. Preparation and certification of Re–Os dating reference materials: molybdenite HLP and JDC. *Geostand. Geoanal. Res.* 28, 41–52.
- Elhlou, S., Belousova, E., Griffin, W.L., Pearson, N.J., O'Reilly, S.Y., 2006. Trace element and isotopic composition of Gj-red zircon standard by laser ablation. *Geochim. Cosmochim. Acta* 70, A158.
- Fu, B., Mernagh, T.P., Kita, N.T., Kemp, A.I.S., Valley, J.W., 2009. Distinguishing magmatic zircon from hydrothermal zircon: a case study from the Gidginbung high sulphidation Au–Ag–(Cu) deposit, SE Australia. *Chem. Geol.* 259, 131–142.
- Gao, J.F., Zhou, M.F., Qi, L., Chen, W., Huang, X.W., 2015. Chalcophile elemental compositions and origin of the Tuwu porphyry Cu deposit, NW China. *Ore Geol. Rev.* 66, 403–421.
- Gao, S., Liu, X.M., Yuan, H.L., Hattendorf, B., Gunther, D., Chen, L., Hu, S.H., 2002. Determination of forty-two major and trace elements in USGS and NIST SRM glasses by laser ablation-inductively coupled plasma-mass spectrometry. *Geostand. Newslett. J. Geostand. Geoanalysis* 26, 191–196.
- Griffin, W., Wang, X., Jackson, S., Pearson, N., O'Reilly, S.Y., Xu, X., Zhou, X., 2002. Zircon chemistry and magma mixing, SE China: in-situ analysis of Hf isotopes, Tonglu and Pingtan igneous complexes. *Lithos* 61, 237–269.
- Gu, L.X., Hu, S.X., Chu, Q., Yu, C.S., Xiao, X.X., Liu, X.Z., 1999. Pre-collision granites and post-collision intrusive assemblage of the Kelameili–Harlik orogenic belt. *Acta Geol. Sin.* 73, 316–329.
- Guan, Q., Zhu, D.C., Zhao, Z.D., Dong, G.C., Zhang, L.L., Li, X.W., Liu, M., Mo, X.X., Liu, Y.S., Yuan, H.L., 2011. Crustal thickening prior to 38 Ma in southern Tibet: evidence from lower crust-derived adakitic magmatism in the Gangdese Batholith. *Gondwana Res.* 21, 88–89.
- Han, C.M., Xiao, W.J., Zhao, G.C., Mao, J.W., Li, S.Z., Yan, Z., Mao, Q.G., 2006. Major types, characteristics and geodynamic mechanism of Upper Paleozoic copper deposits in northern Xinjiang, north western China. *Ore Geol. Rev.* 28, 308–328.
- Han, C.M., Xiao, W.J., Zhao, G.C., Sun, M., Qu, W.J., Du, A.D., 2014. Re–Os geochronology on molybdenites from the Donggebi Mo deposit in the Eastern Tianshan of the Central Asia Orogenic Belt and its geological significance. *Resour. Geol.* 64, 136–148.
- Hopson, C., Wen, J., Tilton, G., Tang, Y., Zhu, B., Zhao, M., 1989. Palaeozoic plutonism in East Junggar, Bogdashan, and eastern Tianshan, NW China. *EOS Trans. Am. Geophys. Union* 70, 1403–1404.
- Hoskin, P.W.O., Ireland, T.R., 2000. Rare earth element chemistry of zircon and its use as a provenance indicator. *Geology* 7, 627–630.
- Hoskin, P.W.O., Schaltegger, U., 2003. The composition of zircon and igneous and metamorphic petrogenesis. *Rev. Mineral. Geochem.* 53, 27–62.
- Hou, T., Zhang, Z.C., Santosh, M., Encarnacion, J., Zhu, J., Luo, W.J., 2014. Geochronology and geochemistry of submarine volcanic rocks in the Yamansu iron deposit, Eastern Tianshan Mountains, NW China: constraints on the metallogenesis. *Ore Geol. Rev.* 56, 487–502.
- Hou, Z.Q., Pan, X.F., Li, Q.Y., Yang, Z.M., Song, Y.C., 2013. The giant Dexing porphyry Cu–Mo–Au deposit in east China: product of melting of juvenile lower crust in an intracontinental setting. *Mineral. Deposita* 48, 1019–1045.
- Huang, X.W., Qi, L., Gao, J.F., Zhou, M.F., 2013. First reliable Re–Os ages of pyrite and stable isotope compositions of Fe–(Cu) deposits in the Hami Region, Eastern Tianshan Orogenic Belt, NW China. *Resour. Geol.* 63, 166–187.
- Jahn, B.M., Wu, F., Chen, B., 2000. Granitoids of the Central Asian orogenic belt and continental growth in the Phanerozoic. *Transactions of the Royal Society of Edinburgh: Earth Sci.* 91, 181–193.
- Jiang, S.H., Nie, F.J., Su, Y.J., Cai, J.X., Ding, Z., 2010. The geological features and origin of the Tumurtin Ovoo large-scale zinc deposit, Mongolia. *Acta Geosci. Sin.* 31, 321–330 (in Chinese with English abstract).
- Le Maitre, R.W., 2002. *Igneous Rocks: A Classification and Glossary of Terms*. second ed. Cambridge University Press, Cambridge, pp. 33–39.
- Lei, R.X., Wu, C.Z., Gu, L.X., Zhang, Z.Z., Chi, G.X., Jiang, Y.H., 2011. Zircon U–Pb chronology and Hf isotope of the Xingxingxia granodiorite from the Central Tianshan zone (NW China): implications for the tectonic evolution of the southern Altaiids. *Gondwana Res.* 20, 582–593.

- Liégeois, J.P., Navez, J., Hertogen, J., Black, R., 1998. Contrasting origin of post-collisional high-K calc-alkaline and shoshonitic versus alkaline and peralkaline granitoids. The use of sliding normalization. *Lithos* 45, 1–28.
- Liu, J.J., Zheng, M.H., Cook, N.J., Long, X.R., Deng, J., Zhai, Y.S., 2007. Geological and geochemical characteristics of the Sawaya'erduan gold deposit, southwestern Chinese Tianshan. *Ore Geol. Rev.* 32, 125–156.
- Liu, Y.F., Nie, F.J., Jiang, S.H., Xue, J., Hou, W.R., Yun, F., 2010. The geochronology and geochemical features of ore-hosting granite in the Arynnuur molybdenum deposit, Mongolia. *Acta Geosci. Sin.* 31, 343–349 (in Chinese with English abstract).
- Ludwig, K.R., 2003. User's manual for Isoplot 3.0, a geochronological tool kit for Microsoft Excel. Berkeley, CA. Geochronological Center Special Publication 4, pp. 25–32.
- Ma, R.S., Wang, Y.Y., Ye, S.F., 1993. Tectonic Framework and Crustal Evolution, East Tianshan. Publishing House of Nanjing University, Nanjing, pp. 1–265 (in Chinese with English abstract).
- Mao, J.W., Zhang, Z., Zhang, Z., Du, A., 1999. Re-Os isotopic dating of molybdenites in the Xiaoliugou W (Mo) deposit in the Northern Qilian mountains and its geological significance. *Geochim. Cosmochim. Acta* 63, 1815–1818.
- Mao, J.W., Goldfarb, R.T., Wang, Y.T., Hart, C.J., Wang, Z.L., Yang, J.M., 2005. Late Paleozoic base and precious metal deposits, East Tianshan, Xinjiang, China: characteristics and geodynamic setting. *Episodes* 28, 1–14.
- Mao, J.W., Pirajno, F., Lehmann, B., Luo, M.C., Berzina, N., 2014. Distribution of porphyry deposits in the Eurasian continent and their corresponding tectonic settings. *J. Asian Earth Sci.* 79, 576–584.
- Miyashiro, A., 1974. Volcanic rock series in island arcs and active continental margins. *Am. J. Sci.* 274, 321–355.
- Pearce, J.A., Harris, N.B.W., Tindle, A.C., 1984. Trace element discrimination diagrams for the tectonic interpretation of granitic rocks. *J. Petrol.* 25, 956–983.
- Pearce, J.A., Peate, D.W., 1995. Tectonic implications of the composition of volcanic ARC magmas. *Annu. Rev. Earth Planet. Sci.* 23, 251–285.
- Pirajno, F., 2010. Intracontinental strike-slip faults, associated magmatism, mineral systems and mantle dynamics: examples from NW China and Altay-Sayan (Siberia). *J. Geodyn.* 50, 325–346.
- Pirajno, F., 2013. The Geology and Tectonic Settings of China's Mineral Deposits. Springer, Berlin, pp. 1–671.
- Pirajno, F., Luo, Z.Q., Liu, S.F., Dong, L.H., 1997. Gold deposits in the Eastern Tian Shan, Northwestern China. *Int. Geol. Rev.* 39, 891–904.
- Pirajno, F., Seltmann, R., Yang, Y.Q., 2011. A review of mineral systems and associated tectonic settings of northern Xinjiang, NW China. *Geosci. Front.* 2, 157–185.
- Qin, K.Z., Fang, T.H., Wang, S.L., Zhu, B.Q., Feng, Y.M., Yu, H.F., Xiu, Q.Y., 2002. Platetectonic division, evolution and metallogenic settings in eastern Tianshan Mountains, NW-China. *Xinjiang Geol.* 20, 302–308 (in Chinese with English abstract).
- Qin, K.Z., Su, B.X., Sakyi, P.A., Tang, D.M., Li, X.H., Sun, H., Xiao, Q.H., Liu, P.P., 2011. SIMS zircon U-Pb geochronology and Sr-Nd isotopes of Ni-Cu bearing mafic-ultramafic intrusions in eastern Tianshan and Beishan in correlation with flood basalts in Tarim basin (NW China): constraints on a ca. 280 Ma mantle plume. *Am. J. Sci.* 311, 237–260.
- Qin, K.Z., Zhang, L.C., Ding, K.S., Xu, Y.X., Tang, D.M., Xu, X.W., Ma, T.L., Li, G.M., 2009. Mineralization type, petrogenesis of ore-bearing intrusions and mineralogical characteristics of Sanchakou copper deposits in eastern Tianshan. *Acta Petrol. Sin.* 25, 845–861.
- Rapp, P.R., Shimizu, N., Norman, M.D., 1999. Applegate, reaction between slab-derived melt and peridotite in the mantle wedge: experimental constrains at 38 GPa. *Chem. Geol.* 160, 335–356.
- Rapp, P.R., Watson, E.B., 1995. Dehydration melting of metabasalt at 8–32 kbar: implications for continental growth and crust–mantle recycling. *J. Petrol.* 36, 891–931.
- Reich, M., Parada, M.A., Palacios, C., Dietrich, A., Schultz, F., Lehmann, B., 2003. Adakite-like signature of Late Miocene intrusions at the Los Pelambres giant porphyry copper deposit in the Andes of central Chile: metallogenetic implications. *Mineral. Deposita* 38, 876–885.
- Richards, J.P., 2003. Tectono-magmatic precursors for porphyry Cu-(Mo-Au) deposit formation. *Econ. Geol.* 98, 1515–1533.
- Rollinson, H.R., 1993. Using Geochemical Data: Evaluation, Presentation, Interpretation. Longman Scientific & Technical, New York, pp. 1–352.
- Rui, Z.Y., Liu, Y.L., Wang, L.S., Wang, Y.T., 2002. The eastern Tianshan porphyry copper belt in Xinjiang and its tectonic framework. *Acta Petrol. Sin.* 76, 83–94 (in Chinese with English abstract).
- Santosh, M., Kusky, T., Wang, L., 2011. Supercontinent cycles, extreme metamorphic processes, and changing fluid regimes. *Int. Geol. Rev.* 53, 1403–1423.
- Sayit, K., Goncuoglu, M.C., 2009. Geochemistry of mafic rocks of the Karakaya complex, Turkey: evidence for plume-involvement in the Palaeoethyan extensional regime during the Middle and Late Triassic. *Int. J. Earth Sci.* 98, 367–385.
- Schaltegger, U., Fanning, C.M., Günther, D., Maurin, J.C., Schulmann, K., Gebauer, D., 1999. Growth, annealing and recrystallization of zircon and preservation of monazite in high-grade metamorphism: conventional and in-situ U-Pb isotope, cathodoluminescence and microchemical evidence. *Contrib. Mineral. Petrol.* 134, 186–201.
- Seedorff, E., Dilles, J.H., Proffett, J.M., Einaudi, M.T., Zurcher, L., Stavast, W.J., Johnson, D.A., Barton, M.D., 2005. Porphyry deposits: characteristics and origin of hypogene features. *Economic Geology* 100th Ann, pp. 251–298.
- Sengör, A.M.C., Natal'in, B.A., Burtman, V.S., 1993. Evolution of the Altaiid tectonic collage and Paleozoic crustal growth in Eurasia. *Nature* 364, 299–307.
- Shen, P., Pan, H.D., Dong, L.H., 2014. Yandong porphyry Cu deposit, Xinjiang, China—geology, geochemistry and SIMS U-Pb zircon geochronology of host porphyries and associated alteration and mineralization. *J. Asian Earth Sci.* 80, 197–217.
- Shen, P., Pan, H.D., Dong, L.H., Yang, J.S., Shen, Y.C., Dai, H.W., Guan, W.N., Zhao, Y.J., 2012. Caldera complex, hosted rocks and alteration of the Yandong porphyry copper deposit in Eastern Tianshan, Xinjiang. *Acta Petrol. Sin.* 28, 1966–1980 (in Chinese with English abstract).
- Shirey, S.B., Walker, R.J., 1995. Carius tube digestion for low-bank rhenium–osmium analysis. *Anal. Chem.* 67, 2136–2141.
- Shu, L., Charvet, J., Guo, L., Lu, H., 1999. A large-scale Paleozoic dextral ductile strike-slip zone: the Aqikkudug–Weiya zone along the northern margin of the Central Tianshan belt, Xinjiang, NW China. *Acta Geol. Sin.* 73, 148–162.
- Shu, L.S., Yu, J.H., Charvet, J., Charvet, L., Sang, H.Q., Zhang, R.G., 2004. Geological, geochemical and geochemical features of granulites in the Eastern Tianshan, NW China. *J. Asian Earth Sci.* 24, 25–41.
- Sillitoe, R.H., 1972. A plate tectonic model for the origin of porphyry copper deposits. *Econ. Geol.* 67, 184–197.
- Sillitoe, R.H., 2010. Porphyry copper systems. *Econ. Geol.* 105, 3–41.
- Smoliar, M.L., Walker, R.J., Morgan, J.W., 1996. Re-Os ages of group IIA, IIIA, IVA and VIB iron meteorites. *Science* 271, 1099–1102.
- Soderlund, U., Patchett, P.J., Vervoort, J.D., Isachsen, C.E., 2004. The ¹⁷⁶Lu decay constant determined by Lu-Hf and U-Pb isotope systematics of Precambrian mafic intrusions. *Earth Planet. Sci. Lett.* 219, 311–324.
- Song, B., Li, J.Y., Li, W.Q., Wang, K.Z., Wang, Y., 2002. SHRIMP dating of zircon from Dananhu and Kezikelasai granitoid batholith in southern margin of Tuiha basin, East Tianshan, NW China and their geological implication. *Xinjiang Geol.* 20, 342–345 (in Chinese with English abstract).
- Su, B.X., Qin, K.Z., Sun, H., Tang, D.M., Sakyi, P.A., Chu, Z.Y., Liu, P.P., Xiao, Q.H., 2012. Subduction-induced mantle heterogeneity beneath Eastern Tianshan and Beishan: insights from Nd-Sr-Hf-O isotopic mapping of Late Paleozoic mafic-ultramafic complexes. *Lithos* 134, 41–51.
- Sun, S.S., McDonough, W.F., 1989. Chemical and isotopic systematics of oceanic basalts, implications for mantle composition and processes. In: Saunders, A.D., Norry, M.J. (Eds.), Magmatism in Ocean Basins. London Geological Society Special Publication 42, pp. 313–345.
- Sun, W.D., Ling, M.X., Yang, X.Y., Fan, W.M., Ding, X., Liang, H.Y., 2010. Ridge subduction and porphyry copper-gold mineralization: an overview. *Sci. China Earth Sci.* 53, 475–484.
- Sylvester, P.J., 1998. Post-collisional strongly peraluminous granites. *Lithos* 45, 29–44.
- Tang, G.J., Wang, Q., Wyman, D.A., Li, Z.X., Zhao, Z.H., Jia, X.H., Jiang, Z.Q., 2010. Ridge subduction and crustal growth in the Central Asian Orogenic Belt: evidence from Late Carboniferous adakites and high-Mg diorites in the western Junggar region, northern Xinjiang (west China). *Chem. Geol.* 277, 281–300.
- Tang, J.H., Gu, L.X., Zhang, Z.Z., Wu, C.Z., San, J.Z., Wang, C.S., Liu, S.H., Zhang, G.H., 2007. Characteristics age and origin of the Xianshuiquan gneissose granite in eastern Tianshan. *Acta Petrol. Sin.* 23, 1803–1820 (in Chinese with English abstract).
- Tang, W.H., Zhang, Z.C., Li, J.F., Li, K., Luo, Z.W., Chen, Y., 2015. Mesozoic and Cenozoic uplift and exhumation of the Bogda Mountain, NW China: evidence from apatite fission track analysis. *Geosci. Front.* 6, 617–625.
- Wan, B., Xiao, W.J., Zhang, L.C., Han, C.M., 2012. Iron mineralization associated with a major strike-slip shear zone: radiometric and oxygen isotope evidence from the Mengku deposit, NW China. *Ore Geol. Rev.* 44, 136–147.
- Wang, J.B., Wang, Y.W., He, Z.J., 2006. Ore deposits as a guide to the tectonic evolution in the East Tianshan Mountains, NW China. *Geol. China* 33, 461–469 (in Chinese with English abstract).
- Wang, Y.H., Xue, C.J., Gao, J.B., Zhang, F.F., Liu, J.J., Wang, J.P., Wang, J.C., 2016a. The genesis of the ores and granitic rocks at the Hongshi Au deposit in Eastern Tianshan, China: constraints from zircon U-Pb geochronology, geochemistry and isotope systematics. *Ore Geol. Rev.* 74, 122–138.
- Wang, Y.H., Xue, C.J., Liu, J.J., Zhang, F.F., 2016b. Geological, geochronological, geochemical, and Sr-Nd-O-Hf isotopic constraints on origins of intrusions associated with the Baishan porphyry Mo deposit in eastern Tianshan. *Mineral. Deposita*, NW China <http://dx.doi.org/10.1007/s00126-016-0646-z>.
- Wang, Y.H., Xue, C.J., Liu, J.J., Wang, J.P., Yang, J.T., Zhang, F.F., Zhao, Z.N., Zhao, Y.J., 2014. Geochronology, geochronology, Hf isotope, and geological significance of the Tuwu porphyry copper deposit in Eastern Tianshan, Xinjiang. *Acta Petrol. Sin.* 30, 3383–3399 (in Chinese with English abstract).
- Wang, Y.H., Zhang, F.F., Liu, J.J., Xue, C.J., Wang, J.P., Liu, B., Lu, W.W., 2015a. Petrogenesis of granites in Baishan molybdenum deposit, eastern Tianshan, Xinjiang: zircon U-Pb geochronology, geochemistry, and Hf isotope constraints. *Acta Petrol. Sin.* 31, 1962–1976 (in Chinese with English abstract).
- Wang, Y.H., Xue, C.J., Liu, J.J., Wang, J.P., Yang, J.T., Zhang, F.F., Zhao, Z.N., Zhao, Y.J., Liu, B., 2015b. Early Carboniferous adakitic rocks in the area of the Tuwu deposit, eastern Tianshan, NW China: slab melting and implications for porphyry copper mineralization. *J. Asian Earth Sci.* 103, 332–349.
- Wang, Y.H., Xue, C.J., Wang, J.P., Peng, R.M., Yang, J.T., Zhang, F.F., Zhao, Z.N., Zhao, Y.J., 2015c. Petrogenesis of magmatism in the Yandong region of Eastern Tianshan, Xinjiang: geochemical, geochronological and Hf isotope Constraints. *Int. Geol. Rev.* 57, 1130–1151.
- Wang, Y.H., Xue, C.J., Zhang, F.F., Liu, J.J., Gao, J.B., Qi, T.J., 2015d. SHRIMP zircon U-Pb geochronology, geochemistry and H-O-Si-Pb isotope systematics of the Kanggur gold deposit in Eastern Tianshan, NW China: implication for ore genesis. *Ore Geol. Rev.* 68, 1–13.
- Wang, Y.H., Zhao, C.B., Zhang, F.F., Liu, J.J., Wang, J.P., Peng, R.M., Liu, B., 2015e. SIMS zircon U-Pb and molybdenite Re-Os geochronology, Hf isotope, and whole-rock geochemistry of the Wunugetushan porphyry Cu-Mo deposit and granitoids in NE China and their geological significance. *Gondwana Res.* 28, 1228–1245.
- Wang, C., Chen, B., Ma, X.H., Yan, X.L., 2015f. Petrogenesis of Early and Late Paleozoic plutons in Sanchakou area of East Tianshan and their implications for evolution of Kangursutse zone. *J. Earth Sci. Environ.* 37, 52–70 (in Chinese with English abstract).
- Watson, E.B., Wark, D.A., Thomas, J.B., 2006. Crystallization thermometers for zircon and rutile. *Contrib. Mineral. Petrol.* 151, 413–433.

- Wei, J.Y., 2015. Discovery and geological implication of the Yuhai Porphyry Cu–Mo deposit in Eastern Tianshan. *Xinjiang Nonferrous Metals*, pp. 34–38 (in Chinese with English abstract).
- Whitehouse, M.J., Platt, J.P., 2003. Dating high-grade metamorphism—constraints from rare earth elements in zircon and garnet. *Contrib. Mineral. Petrol.* 145, 61–74.
- Windley, B.F., Alexeiev, D., Xiao, W., Kröner, A., Badarch, G., 2007. Tectonic models for accretion of the Central Asian Orogenic Belt. *J. Geol. Soc. Lond.* 164, 31–47.
- Wood, D.A., Joron, J.L., Treuil, M., 1979. A re-appraisal of the use of trace elements to classify and discriminate between magma series erupted in different tectonic settings. *Earth Planet. Sci. Lett.* 45, 326–336.
- Wu, F.Y., Li, X.H., Yang, J.H., Zheng, Y.F., 2007. Discussions on the petrogenesis of granites. *Acta Petrol. Sin.* 23, 1217–1238 (in Chinese with English abstract).
- Wu, F.Y., Yang, Y.H., Xie, L.W., Yang, J.H., Xu, P., 2006a. Hf isotopic compositions of the standard zircons and bad-deleyites used in U–Pb geochronology. *Chem. Geol.* 234, 105–126.
- Wu, H., Li, H.Q., Chen, F.W., Lu, Y.F., Deng, G., Mei, Y.P., Ji, H.C., 2006b. Zircon SHRIMP U–Pb dating of plagiogranite porphyry in the Chihu molybdenum–copper district, Hami, East Tianshan. *Geol. Bull. China* 25, 549–552 (in Chinese with English abstract).
- Xiao, B., Chen, H.Y., Hollings, P., Han, J.S., Wang, Y.F., Yang, J.T., Cai, K.D., 2015a. Magmatic evolution of the Tuwu–Yandong porphyry Cu belt, NW China: constraints from geochronology, geochemistry and Sr–Nd–Hf isotopes. *Gondwana Res.* <http://dx.doi.org/10.1016/j.gr.2015.09.003>.
- Xiao, W.J., Zhang, L.C., Qin, K.Z., Sun, S.H.U., Li, J.L., 2004. Paleozoic accretionary and collisional tectonics of the eastern Tianshan (China): implications for the continental growth of Central Asia. *Am. J. Sci.* 304, 370–395.
- Xiao, W.J., Huang, B.C., Han, C.M., Sun, S., Li, J.L., 2010. A review of the western part of the Altaiids: a key to understanding the architecture of accretionary orogens. *Gondwana Res.* 18, 253–273.
- Xiao, W.J., Windley, B.E., Allen, M.B., Han, C.M., 2013. Paleozoic multiple accretionary and collisional tectonics of the Chinese Tianshan orogenic collage. *Gondwana Res.* 23, 1316–1341.
- Xiao, W.J., Santosh, M., 2014. The western Central Asian Orogenic Belt: a window to accretionary orogenesis and continental growth. *Gondwana Res.* 25, 1429–1444.
- Xiao, W.J., Sun, M., Santosh, M., 2015b. Continental reconstruction and metallogeny of the Circum-Junggar areas and termination of the southern Central Asian Orogenic Belt. *Geosci. Front.* 6, 137–140.
- Xue, C.J., Chi, G.X., Li, Z.D., Dong, X.F., 2014. Geology, geochemistry and genesis of the Cretaceous and Paleocene sandstone- and conglomerate-hosted Urgen Zn–Pb deposit, Xinjiang, China: a review. *Ore Geol. Rev.* 63, 328–342.
- Xue, C.J., Chi, G.X., Zhao, X.B., Wu, G.G., Zhao, Z.F., Dong, L.H., 2015. Multiple and prolonged porphyry Cu–Au mineralization and alteration events in the Halaslu deposit, Chinese Altai, Xinjiang, northwestern China. *Geosci. Front.* <http://dx.doi.org/10.1016/j.gsf.2015.10.008>.
- Yang, F.Q., Mao, J.W., Pirajno, F., Yan, S.H., Liu, G.R., Zhou, G., Zhang, Z.X., Liu, F., Geng, X.X., Guo, C.L., 2012. A review of the geological characteristics and geodynamic setting of Late Paleozoic porphyry copper deposits in the Junggar region, Xinjiang Uygur Autonomous Region, Northwest China. *J. Asian Earth Sci.* 49, 80–98.
- Yang, F.Q., Chai, F.M., Zhang, Z.X., Geng, X.X., Li, Q., 2014. Zircon U–Pb geochronology, geochemistry, and Sr–Nd–Hf isotopes of granitoids in the Yulekenhalasu copper ore district, northern Junggar, China: petrogenesis and tectonic implications. *Lithos* 190–191, 85–103.
- Yuan, H.L., Gao, S., Liu, X.M., Li, H.M., Günther, D., Wu, F.Y., 2004. Accurate U–Pb age and trace element determinations of zircon by laser ablation–inductively coupled plasma–mass spectrometry. *Geostand. Geoanal. Res.* 28, 353–370.
- Zang, Y.S., 2014. Geological Characteristics and Tectonic Evolution of Yuhai Porphyry Copper Deposit in Eastern Tianshan. Chang'an University, Xi'an, China, pp. 1–62 (in Chinese with English abstract).
- Zhai, Y.S., Deng, J., Li, X.B., 1999. Essentials of Metallogeny. Geological Publishing House, Beijing, China, pp. 1–287 (in Chinese with English abstract).
- Zhai, Y.S., Yao, S.Z., Cai, K.Q., 2011. Mineral Deposits. third ed. Geological Publishing House, Beijing (in Chinese).
- Zhang, F.F., Wang, Y.H., Liu, J.J., Wang, J.P., Zhao, C.B., Song, Z.W., 2016. Origin of the Wunugetushan porphyry Cu–Mo deposit, Inner Mongolia, NE China: constraints from geology, geochronology, geochemistry, and isotopic compositions. *J. Asian Earth Sci.* 117, 208–224.
- Zhang, F.F., Wang, Y.H., Liu, J.J., Wang, J.P., 2015a. Zircon U–Pb and molybdenite Re–Os geochronology, Hf isotope analyses, and whole-rock geochemistry of the Donggebi Mo deposit, eastern Tianshan, Northwest China, and their geological significance. *Int. Geol. Rev.* 57, 446–462.
- Zhang, F.F., Wang, Y.H., Liu, J.J., 2015b. Petrogenesis of Late Carboniferous granitoids in the Chihu area of Eastern Tianshan, NW China, and tectonic implications: geochronological, geochemical, and zircon Hf–O isotopic constraints. *Int. Geol. Rev.* <http://dx.doi.org/10.1080/00206814.2015.1136800>.
- Zhang, L.C., Shen, Y.C., Ji, J.S., 2003. Characteristics and genesis of Kanggur gold deposit in the eastern Tianshan mountains, NW China: evidence from geology, isotope distribution and chronology. *Ore Geol. Rev.* 23, 71–90.
- Zhang, L.C., Qin, K.Z., Xiao, W.J., 2008. Multiple mineralization events in the eastern Tianshan district, NW China: isotopic geochronology and geological significance. *J. Asian Earth Sci.* 32, 236–246.
- Zhao, Z.Y., Zhang, Z.C., Santosh, M., Huang, H., Cheng, Z.G., Ye, J.C., 2015. Early Paleozoic magmatic record from the northern margin of the Tarim Craton: further insights on the evolution of the Central Asian Orogenic Belt. *Gondwana Res.* 28, 328–347.
- Zhou, T.F., Yuan, F., Zhang, D.Y., Fan, Y., Liu, S., Peng, M.X., Zhang, J.D., 2010. Geochronology, tectonic setting and mineralization of granitoids in Juelutouge area, eastern Tianshan, Xinjiang. *Acta Petrol. Sin.* 26, 478–502 (in Chinese with English abstract).
- Zhu, D.C., Mo, X.X., Wang, L.Q., Zhao, Z.D., Niu, Y.L., Zhou, C.Y., Yang, Y.H., 2009. Petrogenesis of highly fractionated I-type granites in the Zayu area of eastern Gangdese, Tibet: constraints from zircon U–Pb geochronology, geochemistry and Sr–Nd–Hf isotopes. *Sci. China (Series D)* 52, 1223–1239.
- Zhu, D.C., Zhao, Z.D., Niu, Y.L., Mo, X.X., Chung, S.I., Hou, Z.Q., Wang, L.Q., Wu, F.Y., 2011. The Lhasa terrane: record of a microcontinent and its histories of drift and growth. *Earth Planet. Sci. Lett.* 301, 241–255.
- Zhu, D.C., Zhao, Z.D., Niu, Y.L., Dilek, Y., Hou, Z.Q., Mo, X.X., 2013. The origin and pre-Cenozoic evolution of the Tibetan Plateau. *Gondwana Res.* 23, 1429–1454.